

Study of Titan's fall southern stratospheric polar cloud composition with Cassini/CIRS: Detection of benzene ice

S. Vinatier^{a,*}, B. Schmitt^b, B. Bézard^a, P. Rannou^c, C. Dauphin^d, R. de Kok^e, D.E. Jennings^f, F.M. Flasar^f

^a LESIA, Observatoire de Paris, PSL Research University, CNRS, Sorbonne Universités, UPMC Univ. Paris 06, Univ. Paris Diderot, Sorbonne Paris Cité, 5 place Jules Janssen, Meudon 92195, France

^b Université Grenoble Alpes, CNRS, Institut de Planétologie et d'Astrophysique de Grenoble (IPAG), France

^c GSMA, UMR CNRS 6089, Univ. de Reims Champagne-Ardenne, France

^d Institut Villebon - Georges Charpak, Département de Physique - UFR Sciences, Université Paris Sud, Bat. 490, rue Hector Bertioz, Orsay 91400, France

^e Department of Physical Geography, Utrecht University, 3508 TC Utrecht, P.O. Box 80115, The Netherlands

^f NASA/Goddard Space Flight Center, Code 693, Greenbelt, MD, 20771, USA

ARTICLE INFO

Article history:

Received 8 September 2017

Revised 4 December 2017

Accepted 22 December 2017

Available online 24 December 2017

Keywords:

Titan, atmosphere

Infrared observations

Atmospheres, structures

Atmospheres, composition

ABSTRACT

We report the detection of a spectral signature observed at 682 cm^{-1} by the Cassini Composite Infrared Spectrometer (CIRS) in nadir and limb geometry observations of Titan's southern stratospheric polar region in the middle of southern fall, while stratospheric temperatures are the coldest since the beginning of the Cassini mission. In the same period, many gases observed in CIRS spectra (C_2H_2 , HCN , C_4H_2 , C_3H_4 , HC_3N and C_6H_6) are highly enriched in the stratosphere at high southern latitude due to the air subsidence of the global atmospheric circulation and some of these molecules condense at much higher altitude than usually observed for other latitudes. The 682 cm^{-1} signature, which is only observed below an altitude of 300 km, is at least partly attributed to the benzene (C_6H_6) ice ν_4 C–H bending mode. While we first observed it in CIRS nadir spectra of the southern polar region in early 2013, we focus here on the study of nadir data acquired in May 2013, which have a more favorable observation geometry. We derived the C_6H_6 ice mass mixing ratio in 5° latitude bins from the south pole to 65°S and infer the C_6H_6 cloud top altitude to be located deeper with increasing distance from the pole. We additionally analyzed limb data acquired in March 2015, which were the first limb dataset available after the May 2013 nadir observation, in order to infer a vertical profile of its mass mixing ratio in the 0.1–1 mbar region (250–170 km). We derive an upper limit of $\sim 1.5\text{ }\mu\text{m}$ for the equivalent radius of pure C_6H_6 ice particles from the shape of the observed emission band, which is consistent with our estimation of the ice particle size from condensation growth and sedimentation timescales. We compared the ice mass mixing ratio with the haze mass mixing ratio inferred in the same region from the continuum emission of CIRS spectra, and derived that the haze mass mixing ratios are ~ 30 times larger than the C_6H_6 ice mass mixing ratios for all observations. Several other unidentified signatures are observed near 687 and 702 cm^{-1} and possibly 695 cm^{-1} , which could also be due to ice spectral signatures as they are observed in the deep stratosphere at pressure levels similar to the C_6H_6 ice ones. We could not reproduce these signatures with pure nitrile ices (HCN , HC_3N , CH_3CN , $\text{C}_2\text{H}_5\text{CN}$ and C_2N_2) spectra available in the literature except the 695 cm^{-1} feature that could possibly be due to $\text{C}_2\text{H}_3\text{CN}$ ice. From this tentative detection, we derive the corresponding $\text{C}_2\text{H}_3\text{CN}$ ice mass mixing ratio profile and also inferred an upper limit of its gas volume mixing ratio of 2×10^{-7} at 0.01 mbar at 79°S in March 2015.

© 2017 Elsevier Inc. All rights reserved.

1. Introduction

Since the northern spring equinox in August 2009, Titan's stratospheric and mesospheric thermal field and minor species

mixing ratio distributions have experienced very strong seasonal changes. Analysis of the Cassini Composite Infrared Spectrometer (CIRS) showed that the dynamical descending branch predicted by General Circulation Models (Lebonnois et al., 2012; Newman et al., 2011; Larson et al., 2014) was observed at the south pole for the first time in June 2010 through its adiabatic heating that warmed up the mesosphere around 400 km and through enhancement of

* Corresponding author.

E-mail address: sandrine.vinatier@obspm.fr (S. Vinatier).

haze confined at latitudes higher than 80°S (Teanby et al., 2012; Vinatier et al., 2015). This descending branch also brought molecular enriched air from the upper atmosphere, where molecules are formed, towards deeper levels, and the first molecular enhancements were observed above the South pole in June 2011 above 400 km (Teanby et al., 2012; Vinatier et al., 2015; Coustenis et al., 2016). As southern autumn progressed these enhancements were observed at lower altitude due to the downward transport of air by the descending branch. However, while temperature in the upper atmosphere was expected to increase by adiabatic heating due to the predicted reinforcement of the descending branch vertical velocity, an unexpected thermal cooling was observed in January 2012 in the 350–500 km range (de Kok et al., 2014; Vinatier et al., 2015; Teanby et al., 2017; Vinatier et al., 2016). This cooling is partly due to the radiative cooling by the highly enriched molecules at high altitude, which exceeds the adiabatic heating due to the descending branch (Teanby et al., 2017). Additionally, another factor explaining the temperature decrease is the decrease of solar flux during southern autumn. This results in a net cooling of the high southern latitudes, with observed temperatures as low as 115 K in the deep stratosphere (Achterberg et al., 2014), which leads to condensation of gas at higher altitude than usually observed for other latitudes. HCN ice was detected at 300 km in June 2012 from the Visual and Infrared Mapping Spectrometer (VIMS) limb observations (de Kok et al., 2014), coincident with the stratospheric polar cloud observed since May 2012 by the Cassini Imaging Science Subsystem (West et al., 2016) located at the same altitude and with a similar horizontal extent (~600–900 km). This suggests that HCN ice could be an important component of the autumn south polar cloud. Additionally, in July 2012, CIRS first observed the 220 cm⁻¹ emission feature, attributed to condensates (Coustenis et al., 1999; de Kok et al., 2007; 2008), at the south pole (while it was not observed in February 2012, (Jennings et al., 2012)). All these independent observations suggest a rapid formation of the stratospheric polar cloud between February and May 2012. In the present study, we investigate the composition of the south polar cloud using CIRS nadir and limb observations in the 600–1400 cm⁻¹ wavenumber range in May 2013 (from nadir viewing) and in March 2015 (from limb viewing). We present here the detection of the ν_4 benzene (C₆H₆) ice C–H bending vibration band at 682 cm⁻¹ (Bertie and Keefe, 2004) and derive spatial constraints of its mass mixing ratio in May 2013 and its vertical extent in March 2015.

Section 2 describes observations used in this study. The retrieval method and the inferred temperature and C₆H₆ gas volume mixing ratio profiles are presented in Section 3 and 4, respectively. Section 5 and 6 focus on the detection and retrieval of the C₆H₆ ice mass mixing ratio, respectively. Our results are discussed in Section 7.

2. Observations

CIRS observes the Titan thermal emission in the ranges 10–100 cm⁻¹ with focal plane 1 (FP1), 600–1100 cm⁻¹ with focal plane 3 (FP3) and 1100–1500 cm⁻¹ with focal plane 4 (FP4). We focus here on spectra acquired by FP3 and FP4. Both focal planes are each composed of a linear 10 adjacent detectors array, each detector having a 0.275 × 0.275 mrad field-of-view. During a limb observation, the projected FP3 and FP4 detector arrays are positioned perpendicular to the surface so that each detector probes a different altitude range in the 10–0.001 mbar (100–500 km) region, above a given latitude with a typical 30 km vertical resolution, comparable to the pressure scale height (~40 km in the stratosphere). CIRS also acquires spectra with nadir geometry viewing, in sequences providing the global horizontal mapping during a given flyby, albeit probing the 10–1 mbar region (~100–150 km)

with poor or no vertical resolution. Our study is based on analysis of CIRS nadir spectra acquired at 2.8 cm⁻¹ spectral resolution and limb spectra acquired at 0.5 cm⁻¹ resolution.

2.1. Nadir observations in May 2013

Between September 2012 (T86) and October 2014 (T106), Cassini orbits were highly inclined, with inclination higher than 40° relative to the Saturn equatorial plane. Such inclined orbits are the most suitable to map Titan's poles in nadir observing mode, while simultaneous CIRS limb observations of these regions are impossible. In the present study, we chose to focus on data acquired in May 2013 (Titan's flyby T91) corresponding to the Cassini most inclined orbit in the period September 2012–October 2014. Our selected May 2013 nadir observations were acquired during a flyby with an orbit inclination higher than 60°. The only higher inclined orbit of the mission occurred in January 2017, a few months before the end of the mission.

In order to derive information on the spatial distribution of the south polar cloud, we used nadir observations of the south polar region acquired with the smallest possible emission angle in order to reduce mixing of thermal emission from several latitudes along the line-of-sight, as the temperature latitudinal gradient near the South pole in autumn is strong.

In order to increase signal-to-noise ratio, we averaged observed nadir spectra in latitudinal bins of 5° wide and in emission angle bins of ~10–20° wide with the smallest possible mean emission angle, assuming no longitudinal variations in each 5° bin.

Our spectra selections take into account the 4.1° offset of the stratospheric rotation axis relative to the solid body rotation axis (Achterberg et al., 2008) and its longitudinal drift of 9.15° per year in the sun-fixed frame derived by Achterberg et al. (2011) from data acquired up to the northern spring equinox. In other words, the direction of the stratospheric rotation axis seems to be stationary in the stellar-fixed frame and we define our latitude from this axis. At the equinox, in August 2009, Achterberg et al. (2011) derived an offset azimuth ~95°W from the subsolar longitude. From these results, we estimated that the north pole offset pointed towards a direction ~130°W from the subsolar longitude for our observations in May 2013.

The sub spacecraft latitude and longitude of observations used in this study were about 48°S and 250°W, respectively.

Table 1 gives characteristics of our selected spectra for each 5° latitudinal bin. Spectra were extracted from the v4.3.1 calibration version. Observed FP4 averaged spectra are displayed in Fig. 1, while observed FP3 averages are displayed in Fig. 2.

2.2. Limb observations in March 2015

After February 2012, when the south polar stratospheric composition was probed with CIRS limb observations (Teanby et al., 2012; Vinatier et al., 2015), Cassini's high orbit inclinations prevented us to observe poles with limb viewing geometry till January 2015. We used here the first limb observation of the south polar region acquired at 0.5 cm⁻¹ spectral resolution after our May 2013 nadir selection. These limb spectra were acquired in March 2015, during Titan flyby T110 (see their characteristics in Table 2). In order to probe the deep stratospheric temperatures, we combined our limb spectra analysis with a nadir spectra average acquired at 3 cm⁻¹ spectral resolution in December 2014, during flyby T107, assuming that no temporal variations occurred in the deep stratosphere (around 10 mbar) between December 2014 and March 2015 (~6 Titan's days), which is justified regarding the radiative relaxation time of ~10⁷ s (~36 Titan's days) at 10 mbar derived by Bézard et al. (2017) for equatorial temperature (radiative relaxation

Table 1

Characteristics of the averaged nadir spectra acquired at a spectral resolution of 2.8 cm^{-1} . θ is the emission angle. Spectra were extracted from the 4.3.1 version of the CIRS database. Latitudes are those corresponding to the solid body latitudes extracted from the CIRS database.

	θ range ($^{\circ}$)	longitude range ($^{\circ}$ W)	number of spectra	mean θ ($^{\circ}$)	Cassini distance to surface (km)	Spatial resolution ($^{\circ}$ latitude)
24th May 2013						
90°S–85°S						
FP3	39.2–48.0	6.9–219.2	17	43.6	361,742	2.19
FP4	39.8–48.7	56.1–353.6	19	44.2	361,483	2.20
85°S–80°S						
FP3	34.8–49.1	139.2–352.0	29	40.9	360,239	2.19
FP4	34.6–50.6	131.0–348.9	27	40.2	360,700	2.19
80°S–75°S						
FP3	29.7–53.7	134.0–359.4	49	38.4	360,625	2.19
FP4	29.6–52.8	137.2–350.9	41	38.1	360,854	2.19
75°S–70°S						
FP3	24.4–56.9	133.4–358.0	76	36.5	360,811	2.19
FP4	24.5–55.9	134.6–356.8	65	37.1	360,333	2.19
70°S–65°S						
FP3	20.2–39.3	186.5–324.3	58	28.5	360,568	2.19
FP4	20.5–39.7	187.2–324.0	51	29.2	360,219	2.18
65°S–60°S						
FP3	20.3–39.8	187.9–325.0	59	29.6	358,945	2.18
2.18 FP4	20.0–39.6	187.6–324.7	56	29.8	355,775	2.16
55°S–50°S						
FP3	4.2–19.8	225.2–283.9	163	10.1	405,761	2.46
FP4	4.3–19.6	225.4–284.1	45	11.9	362,164	2.20
10th December 2014						
80°S–75°S						
FP3	44.7–60.6	5.6–357.8	40	51.3	326,030–306,569	1.86–1.98
FP4	44.5–61.6	8.2–357.6	35	52.0	325,484–307,112	1.86–1.98

Table 2

Characteristics of the averaged limb spectra acquired at a spectral resolution of 0.5 cm^{-1} on 16 March 2015 (flyby T110, solar longitude of 66°). The first four columns give the focal plane, the mean latitude, longitude and vertical resolution of the averaged limb spectra. Fifth column gives the minimum and maximum altitudes of the line-of-sight of averaged spectra. Last column gives the minimum and maximum number per averaged spectra. Spectra were extracted from the 4.3.1 version of the CIRS database.

Focal plane	Mean lat.	Mean long.	Mean vert. resolution (km)	Altitude range (km)	Number of averaged spectra
FP4	79°	135° W	42	123–549	53–134
FP3	81°	137° W	42	128–548	50–124

time would be longer for the observed colder polar temperatures assuming comparable atmospheric composition at 10 mbar).

3. Temperature profiles in the south polar region

3.1. Retrieval method

Intensities of molecular thermal emission bands displayed in Figs. 1 and 2 strongly depend on temperature. We therefore first derived the temperature vertical profile by fitting the ν_4 CH_4 band at 1305 cm^{-1} (see Fig. 1 for May 2013 nadir observations), assuming a CH_4 volume mixing ratio constant with altitude and latitude and equal to 1.48% (Niemann et al., 2010). We used a linear constrained inversion algorithm described by Vinatier et al. (2007a, 2015) to retrieve simultaneously temperature and haze optical depth. A first estimation of the haze optical depth was inferred from the $1070\text{--}1110\text{ cm}^{-1}$ region, but as it was poorly constrained at very high latitude, because of the poor signal-to-noise ratio due to low stratospheric temperature, we corrected it in a second step by fitting the continuum of the $640\text{--}660\text{ cm}^{-1}$ spectral region of the FP3 focal plane (see Section 4) in order to obtain the best fit of the FP3 continuum. We used the aerosol spectral dependence derived by Vinatier et al. (2012).

Our inversion method needs a priori profiles for both temperature and aerosol optical depth. For analysis of May 2013 nadir spectra, these a priori profiles were similar to those derived from limb observations of February 2012 (Vinatier et al., 2015), which were constrained in the $5\text{--}0.001$ mbar range ($\sim 150\text{--}500$ km) with a vertical resolution of ~ 40 km. These vertical profiles of the south polar region are the closest in time to the May 2013 nadir observation as no limb data of the south pole were acquired between February 2012 and January 2015 because of the high inclined Cassini's orbits. For nadir geometry, thermal emission is integrated along the line-of-sight and, for a given wavelength, the region of maximum emission is localized where opacity is close to 1. Nevertheless, some vertical information can be retrieved by simultaneously fitting the methane P-branch (wavenumbers lower than 1290 cm^{-1}), which probes the deep stratosphere in the $0.5\text{--}20$ mbar, and the Q-branch (at 1305 cm^{-1}), which is more opaque and probes lower pressure levels, typically in the $0.05\text{--}1$ mbar region. Then, by fitting the P and Q-branches of the CH_4 ν_4 band, we were able to derive information on the temperature profile from 0.05 to 20 mbar.

The thermal profiles and haze optical depth derived from the May 2013 78°S nadir observations were used as a priori of the retrieval of combined nadir and limb data acquired in Decem-

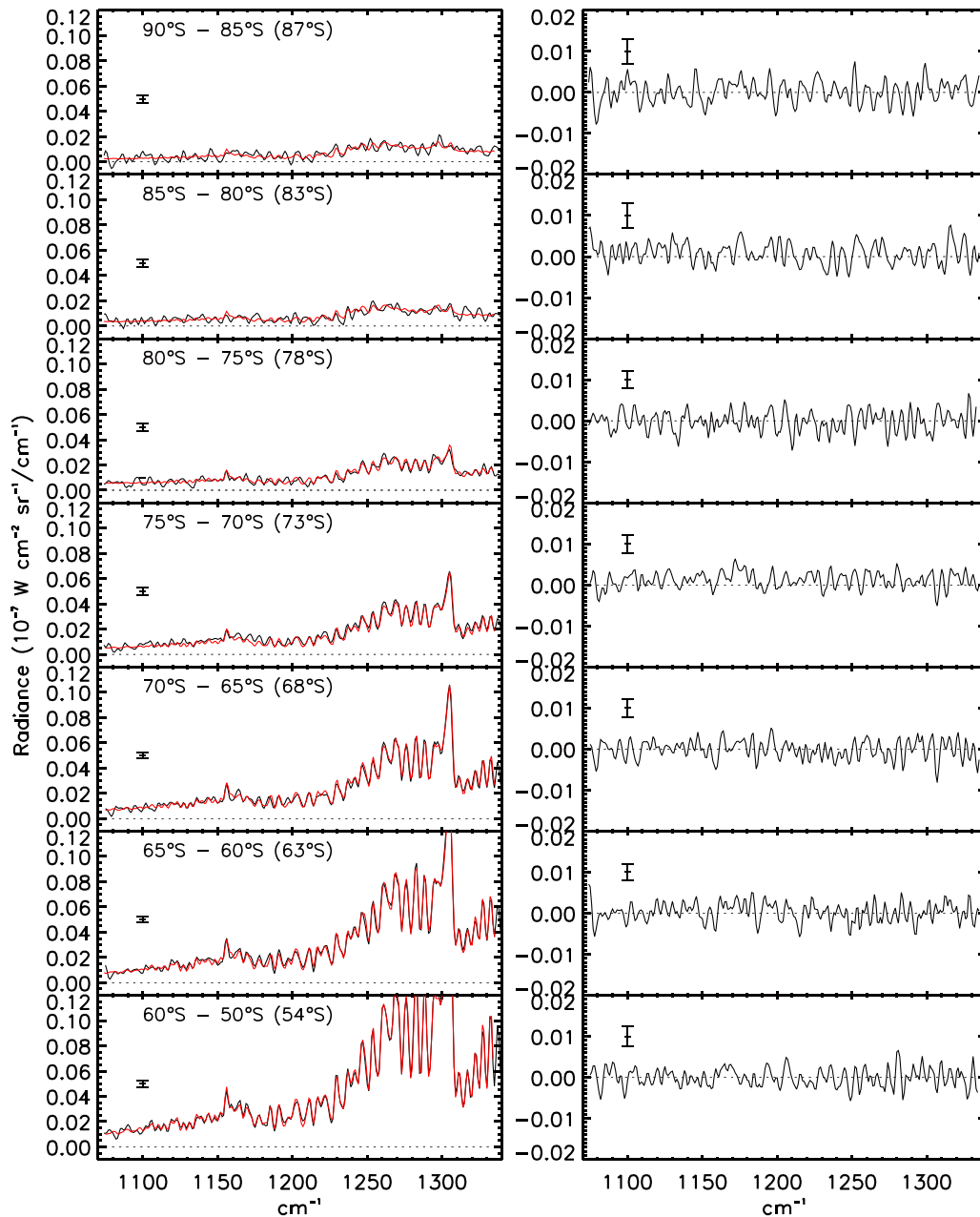


Fig. 1. Left: CIRS spectra (black line) of the CH_4 ν_4 band compared to the calculated spectra (red) from 87°S to 54°S (upper to lower panel) for the nadir observation of May 2017. Latitude ranges used for the averages are given for each observed spectrum (with the mean latitude in brackets). Radiance scale is the same for all latitudes in order to emphasize the latitudinal variations of the CH_4 radiance, which monitors the meridional thermal changes as CH_4 mixing ratio is supposed to be constant. Right: Corresponding residuals (observed spectrum minus calculated spectrum) with $1\text{-}\sigma$ error bars. (For interpretation of the references to colour in this figure legend, the reader is referred to the web version of this article.)

ber 2014 and March 2015, respectively. Usually, in order to obtain the best fit of the ν_4 CH_4 band in limb spectra, we have to apply a shift on the altitude of line-of-sights extracted from the CIRS database. As explained in Vinatier et al. (2007a), this shift is due to the CIRS navigation pointing error and/or the calculated pressure/altitude grid from hydrostatic equilibrium based on our a priori thermal profile outside the regions probed by CIRS. For our previous limb data analysis, we applied shifts usually varying from -30 km to $+30$ km with error bars lower than 5 km (Vinatier et al., 2010, 2015). For the limb data used in this study, because of smaller signal-to-noise due to lower temperatures than usually observed, the shift is poorly constrained and we derived best fits of the ν_4 CH_4 band with a lower limit of $+15$ km (at $3\text{-}\sigma$), a best fit value of $+40$ km, and no real constraint on its upper limit. We

thus applied a $+40$ km vertical shift on all line-of-sight altitudes of our selected limb spectra.

3.2. Results

Calculated spectra corresponding to the best fit of the observed nadir spectra acquired in May 2013 are displayed in Fig. 1 (left panel), with their corresponding residuals (observed spectrum minus calculated one) displayed on the right panel.

Fig. 3(a) shows the retrieved thermal profiles around the south pole in May 2013, with regions of maximum information displayed as solid lines. The 10 mbar level (~ 100 km) does not show strong meridional variations with temperatures in the $125\text{--}135$ K range from 87°S to 54°S , while at 1 mbar (~ 170 km) we observe

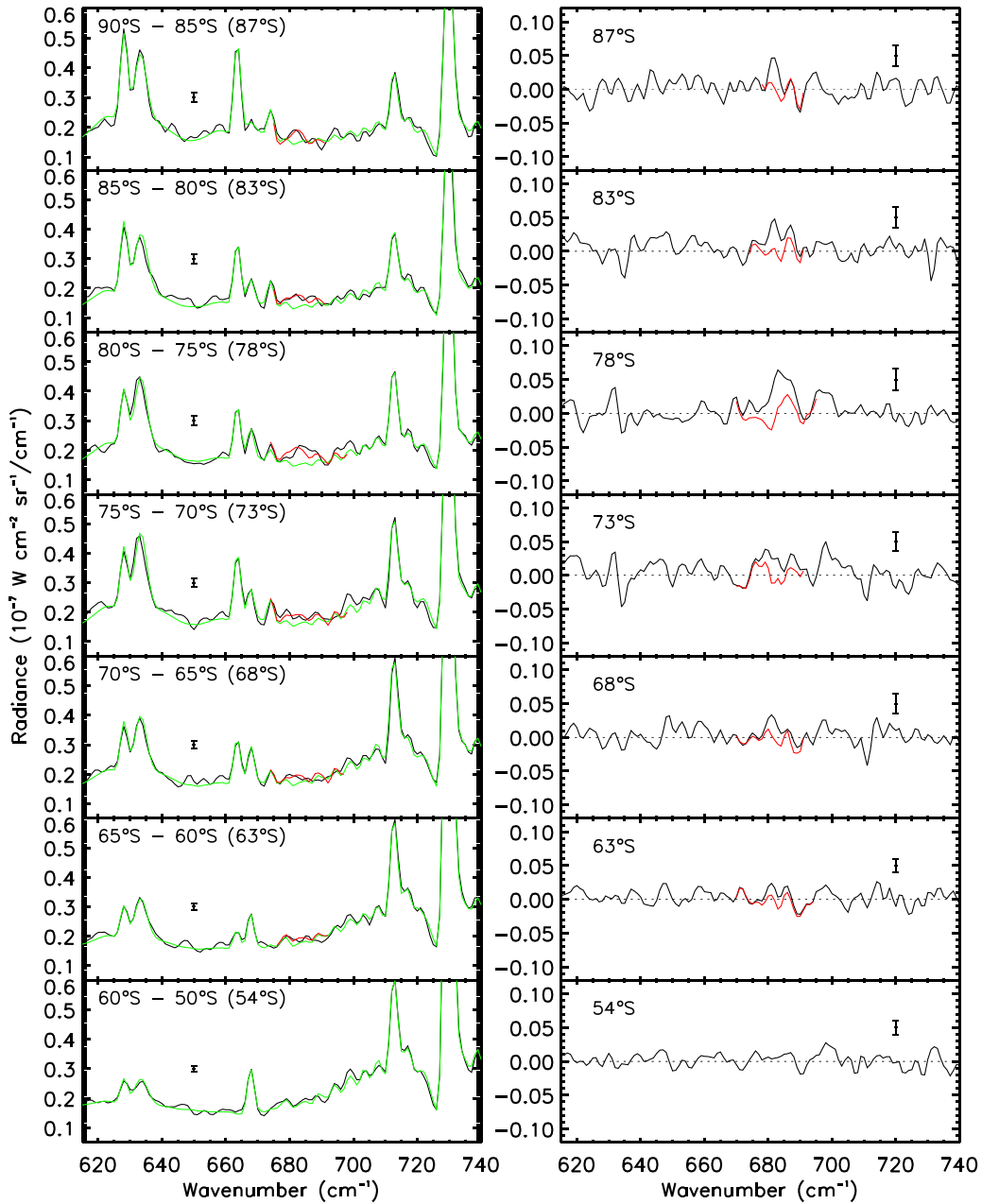


Fig. 2. CIRS nadir spectra in May 2013 (black line) of the 615–740 cm^{-1} region compared to the calculated spectra without C_6H_6 ice (green) from 87°S to 54°S and including the C_6H_6 ice signature (red). Latitude ranges and mean latitude in brackets are given for each observed spectrum. Right: Corresponding residuals (observed spectrum minus calculated spectrum) without C_6H_6 ice (black) and including C_6H_6 ice (red). 1- σ error bars are given for each spectrum. (For interpretation of the references to colour in this figure legend, the reader is referred to the web version of this article.)

much larger meridional variations with a temperature increase from 117 K at latitudes higher than 80°S to 158 K at 54°S. We derive a thermal inversion in the 10–0.5 mbar region at latitudes higher than 80°S that is not observed for higher southern latitudes. A comparable thermal inversion was observed during the northern winter at high northern latitudes with a ~ 1 km vertical resolution from Cassini radio occultation data (Schinder et al., 2012).

Fig. 3(b) displays the thermal profile at 79°S derived in early 2015 combining limb observations of March 2015 probing the 0.03–0.002 mbar region and nadir observations of December 2014 probing the 0.2–20 mbar region. At this latitude, temperatures derived deeper than the 0.2 mbar (~ 215 km) level are colder in early 2015 than in May 2013. For instance, between May 2013 and early 2015, temperature decreased by 15 K at 0.5 mbar and by 10 K at 10 mbar (~ 100 km).

In May 2013 and early 2015, in the 80°S–90°S region, we retrieve stratospheric temperatures of 115 K around 0.5 mbar, which corresponds to the coldest temperature that has been observed for these pressure levels over the entire Cassini mission.

4. Gas mixing ratio retrievals

4.1. Retrieval from nadir spectra acquired in May 2013

The retrieved temperature profiles displayed in Fig. 3(a) were used to reproduce the thermal emission of gas ro-vibrational bands observed in spectra acquired by the CIRS FP3 focal plane. Gas emission bands of C_2H_2 (730 cm^{-1}), C_4H_2 (628 cm^{-1}), $\text{CH}_3\text{C}_2\text{H}$ (633 cm^{-1}), C_6H_6 (674 cm^{-1}), HCN (713 cm^{-1}), HC_3N (663 cm^{-1}) and CO_2 (668 cm^{-1}) are visible on the observed spectra displayed

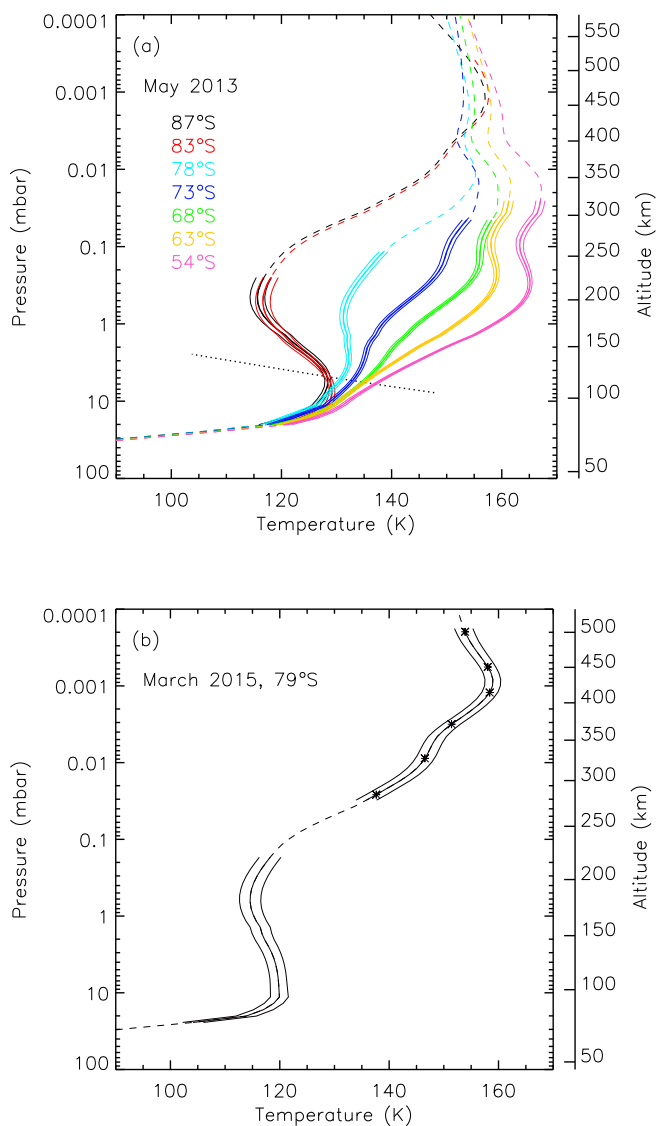


Fig. 3. (a): Thermal profiles around the south pole in May 2013. Altitude scale refers to the 78°S latitude. Thermal profiles relax to the a priori ones in regions without information (dashed lines). Dotted line represents the dry adiabatic lapse rate. (b) Thermal profile at 79°S derived from 6 limb spectra, with tangent heights symbolized as crosses, and one nadir spectrum acquired in December 2014 at the same latitude, probing the pressure levels between 20 and 0.1 mbar. Dashed lines give regions without information from CIRS data. (For interpretation of the references to colour in this figure legend, the reader is referred to the web version of this article.)

in Fig. 2 (left). An inversion algorithm described by Vinatier et al. (2007a, 2015) was used to retrieve molecular volume mixing ratios from the fits of molecular emission bands and haze optical depth from the fit of the continuum. The haze optical depth was retrieved from the 600–620 cm^{-1} and 640–660 cm^{-1} spectral regions, using the spectral dependence of Vinatier et al. (2012). Among molecules listed above, C_2H_2 is the only one for which we can derive vertical information from nadir spectra as it displays well defined P, Q and R-branches, with different opacities probing different pressure regions. For the other molecules, which display a single Q branch, it is not possible to constrain a vertical distribution. The choice of the a priori mixing ratio profiles therefore has an impact on the retrieved mixing ratios. Since June 2011, strong temporal variations were observed above the South pole. Strong enhancements of molecular gas volume mixing ratios were first observed in the 450–500 km region, and then gradually

moved towards deeper levels, due to transport by the descending branch of the global circulation cell and confinement of the polar vortex (Teany et al., 2012; Vinatier et al., 2015; Achterberg et al., 2014). For inversions of nadir spectra at latitudes higher than 80°S, we used, as a priori vertical profiles, those that we retrieved from limb spectra acquired in September 2011 at 85°S (Vinatier et al., 2015) and in March 2015 at 79°S in the present study. For latitudes lower than 65°S, we used as a priori, the profiles that we derived in February 2012 at 46°S from limb spectra as they are more representative of the vertical profiles outside the polar vortex. Best fits of the averaged nadir spectra are displayed in Fig. 2 (left panel) with their corresponding residuals (observed radiance minus calculated one) on the right panel.

4.2. Spatial distribution of C_6H_6 gas mass mixing ratio at high southern latitude in May 2013

The C_6H_6 gas mass mixing ratios derived for the seven latitudinal beams between 90°S and 65°S are displayed in Fig. 4 (black line) as well as their 1- σ envelopes (dotted lines) that include spectral noise contribution and uncertainty on temperature. Benzene gas emission band at 674 cm^{-1} is not detected in the 65–50°S region (see Fig. 2). At levels deeper than the saturation level (level where the mixing ratio profile intercepts the saturation curve displayed as a pink dashed line), benzene mass mixing ratio profiles follow the saturation law of Fray and Schmitt (2009), calculated using the temperature profiles of Fig. 2(a). In the 90–80°S region, benzene saturation occurs at very unusually low pressure levels around 0.03 mbar (280 km), while for lower latitudes, it is observed deeper and deeper with saturation levels located at 0.2 mbar (~230 km) at 78°S, 1 mbar (170 km) at 73°S and 5 mbar (120 km) at 68°S. These saturation levels are unusually high as benzene is predicted to condense around 80 km at mid-latitudes (Barth, 2017).

4.3. Retrieval from limb spectra acquired in March 2015 at 79°S

We used the retrieved temperature profile displayed in Fig. 3(b) to retrieve the vertically resolved profiles of molecular gas mixing ratios from limb spectra acquired in March 2015. We applied a shift of +40 km on the limb spectra line-of-sight altitudes extracted from the CIRS database, as derived from the best fit of the CH_4 band in the thermal profile retrieval step (see Section 3.1).

We infer molecular mixing ratios highly enhanced for all molecules (Vinatier et al., 2016), typically by a factor 5–10 compared to what we derived near the south pole in September 2011 and February 2012 (Vinatier et al., 2015). This is in agreement with results obtained by Teany et al. (2017). We only present here results regarding benzene, while we will present mixing ratios profiles of other molecules in a future paper focusing on the seasonal variations of all molecular mixing ratios during the northern spring.

Fig. 5 displays the fit of the limb spectra acquired at high altitude in March 2015, where the C_6H_6 gas emission band is optically thin.

4.4. Benzene gas mass mixing ratio vertical profile in March 2015 at 79°S

Fig. 6 displays the retrieved C_6H_6 gas mass mixing ratio profile in the upper stratosphere and mesosphere in March 2015 at 79°S. Molecular mixing ratios are so large in March 2015 that only the highest limb spectra, acquired above the 0.003 mbar level (~360 km), are optically thin. Deeper limb spectra have an optically thick contribution that probes in front of the limb tangent

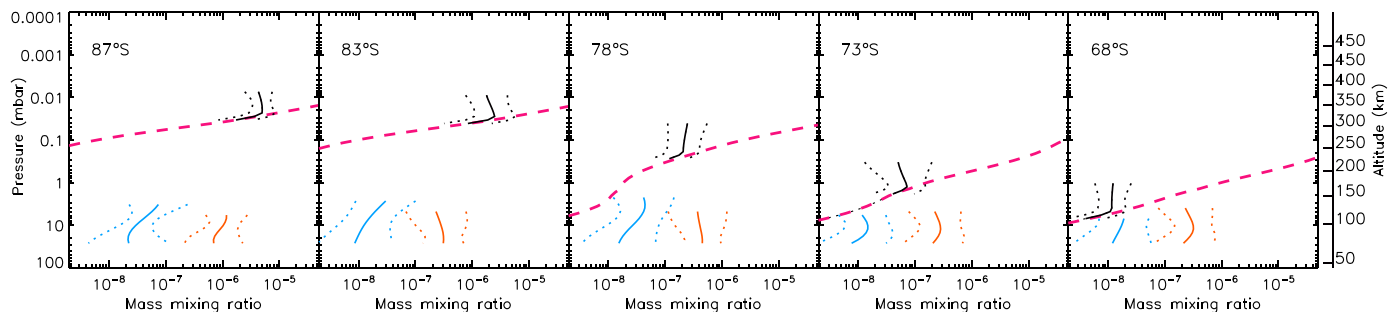


Fig. 4. Retrieved mass mixing ratio of C_6H_6 gas (black) with the saturation curves for each latitude displayed in pink dashed lines. The retrieved haze and C_6H_6 ice mass mixing ratios are displayed in orange and blue, respectively. Solid lines give the mean mass mixing ratio, while the dotted lines give the $1-\sigma$ error bars. The vertical altitude scale corresponds to the $68^\circ S$ latitude. (For interpretation of the references to colour in this figure legend, the reader is referred to the web version of this article.)

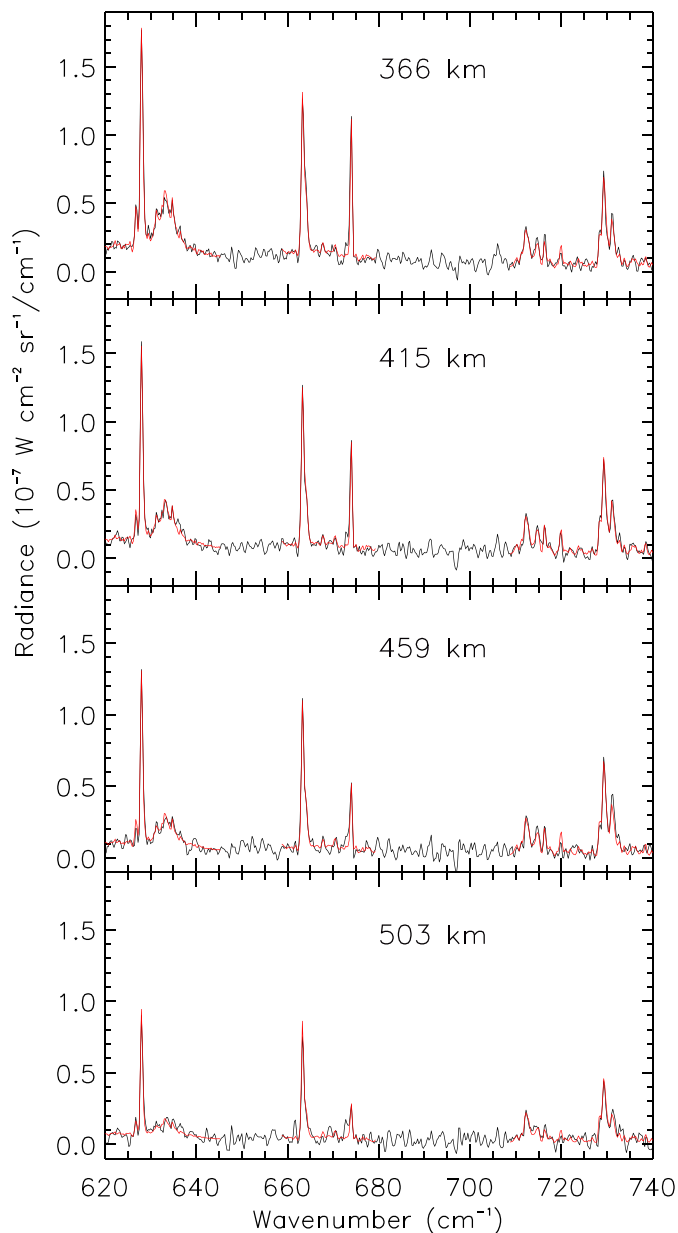


Fig. 5. CIRS limb spectra at $79^\circ S$ in March 2015 (black line) of the $615\text{--}740\text{ cm}^{-1}$ region compared to the calculated spectra (red). Altitudes of the averaged spectra take into account the $+40\text{ km}$ shift related to the altitude given in the CIRS database. (For interpretation of the references to colour in this figure legend, the reader is referred to the web version of this article.)

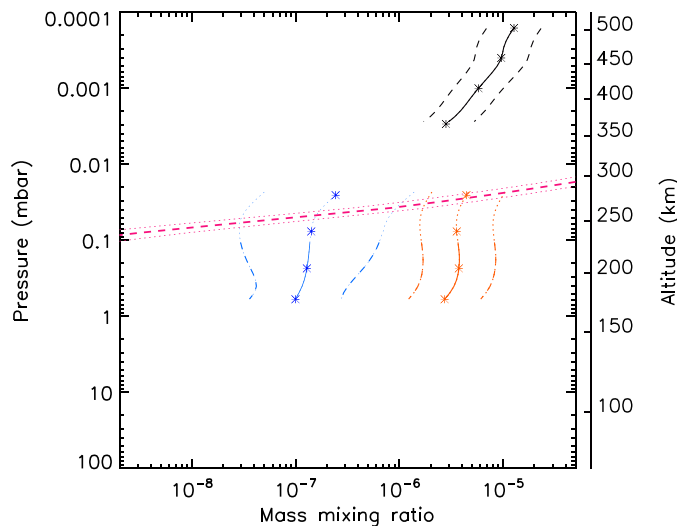


Fig. 6. Retrieved C_6H_6 gas mass mixing ratio profile (black line) from the $79^\circ S$ in March 2015 limb spectra of Fig. 5 with the calculated saturated mass mixing ratio in pink dashed lines. The retrieved haze and C_6H_6 ice mass mixing ratios profiles are displayed in orange and blue, respectively. Altitudes of the line-of-sights of the mean limb spectra are displayed as crosses. Solid lines give the mean mass mixing ratios, while dotted lines give the $1-\sigma$ error bars. (For interpretation of the references to colour in this figure legend, the reader is referred to the web version of this article.)

point along the line-of-sight, which corresponds to thermal emission coming from lower latitudes. We therefore plotted the C_6H_6 gas mass mixing ratio in the $(0.1\text{--}3)\times 10^{-3}$ mbar region.

We derived a gas mass mixing ratio that increases from 3×10^{-6} at 0.003 mbar ($\sim 360\text{ km}$) to 1×10^{-5} at 3×10^{-4} mbar ($\sim 460\text{ km}$). The C_6H_6 gas mass mixing ratio observed at 0.003 mbar is comparable to the values derived from nadir observations at $83^\circ S$ and $87^\circ S$ in May 2013.

5. Benzene ice spectral signature

5.1. Detection

As seen from fits and residuals of our fits of nadir spectra of May 2013 displayed in Fig. 2, calculated spectra (displayed in green) including gas emissions of C_4H_2 , CH_3C_2H , HC_3N , CO_2 , C_6H_6 , HCN and C_2H_2 do not reproduce the $675\text{--}685\text{ cm}^{-1}$ and $692\text{--}702\text{ cm}^{-1}$ spectral ranges, with a larger misfit for higher latitudes for the $675\text{--}685\text{ cm}^{-1}$ feature. We believe that the $692\text{--}702\text{ cm}^{-1}$ spectral signature is similar to the one observed by Voyager at $70^\circ N$ (Coustonis et al., 1999). We also observed this signature with CIRS at the north pole during the northern winter. Its origin is cur-

rently unknown and we will not consider it further in our analysis. Our study presents the first observation of the 682 cm^{-1} spectral signature. The only gas expected in Titan's atmosphere to display a spectral signature at this wavenumber is $\text{C}_2\text{H}_3\text{CN}$ but its Q-branch is too narrow ($\sim 2\text{ cm}^{-1}$) to reproduce the 682 cm^{-1} spectral signature. The fact that it is only observed at the latitudes of coldest temperatures and has a relatively large width of $\sim 10\text{ cm}^{-1}$ supports a vibrational mode of an ice as a spectroscopic candidate. Indeed, 682 cm^{-1} is the wavenumber of a vibrational mode of the C_6H_6 ice. At the south pole, C_6H_6 gas volume mixing ratio is enhanced by several orders of magnitude compared to lower latitudes where we usually derive upper limits of 0.3 ppb in the 2–5 mbar region (Vinatier et al., 2015). In the equatorial region, C_6H_6 gas condenses around 80 km (Barth, 2017), while near the South pole, the combination of low temperature and high C_6H_6 gas volume mixing ratio makes this gas saturating around 0.03 mbar ($\sim 280\text{ km}$) at latitudes higher than 80°S (see Fig. 4). Additionally, the 682 cm^{-1} spectral signature is only seen at latitudes where the C_6H_6 gas emission is observed. All of these arguments reinforce the interpretation of the 682 cm^{-1} feature as due to, at least partly, C_6H_6 ice.

5.2. Model of the C_6H_6 ice spectral signature

Thin films of solid pure C_6H_6 were condensed at 130 K (to insure crystallinity of the sample) from pure C_6H_6 gas in the cryogenic cell fitted in the FTIR spectrometer located at Institut de Planétologie et d'Astrophysique de Grenoble, France (Quirico and Schmitt, 1997). The film thickness was monitored by He-Ne laser interference. Transmission spectra over the mid-IR ($400\text{--}4500\text{ cm}^{-1}$) have been recorded at 1 cm^{-1} resolution between 130 and 20 K. Four main groups of bands were observed with one strong band around 680 cm^{-1} attributed to the ν_4 C-H bending mode (Bertie and Keefe, 2004). This band is asymmetric with a width of about 6.5 cm^{-1} and its peak has a blended double structure at 679 and 681 cm^{-1} . Their positions are only very weakly sensitive with temperature (shift $< 0.5\text{ cm}^{-1}$ between 60 and 130 K). A weaker band (integrated intensity 20 times less) at 705.5 cm^{-1} and another pair of bands at 1032 and 1038.5 cm^{-1} (ν_{14} C-H bending modes) are present in the CIRS spectral range.

In order to derive the spectral dependence of the real refractive index of C_6H_6 ice, we applied a subtractive Kramers–Kronig algorithm constrained with a visible real refractive index $n_r = 1.54$ at 632.8 nm , derived by Romanescu et al. (2010). Real and imaginary indices (Schmitt et al., 2005) are available in the GhoSST (Grenoble Astrophysics and Planetology Solid Spectroscopy and Thermodynamics) database of the SSHADE (Solid Spectroscopy Hosting Architecture of Databases and Expertise) database infrastructure¹.

Fig. 7 displays the spectral dependences of pure C_6H_6 ice extinction (top), absorption (middle) and scattering (bottom) cross sections per unit particle volume for spherical particles with different radii from 0.1 to $4\text{ }\mu\text{m}$.

For ice particles with radii smaller than $1.0\text{ }\mu\text{m}$, scattering is negligible and the extinction per unit particle volume does not depend on the particle radius. For radii larger than $1\text{ }\mu\text{m}$, scattering contribution is not negligible, which results in a change of the band shape more pronounced for particles with radii equal or larger than $1.5\text{ }\mu\text{m}$, resulting in poor fit of the 682 cm^{-1} emission band. We choose here to model the C_6H_6 ice grains by spheres of $0.5\text{ }\mu\text{m}$ radius.

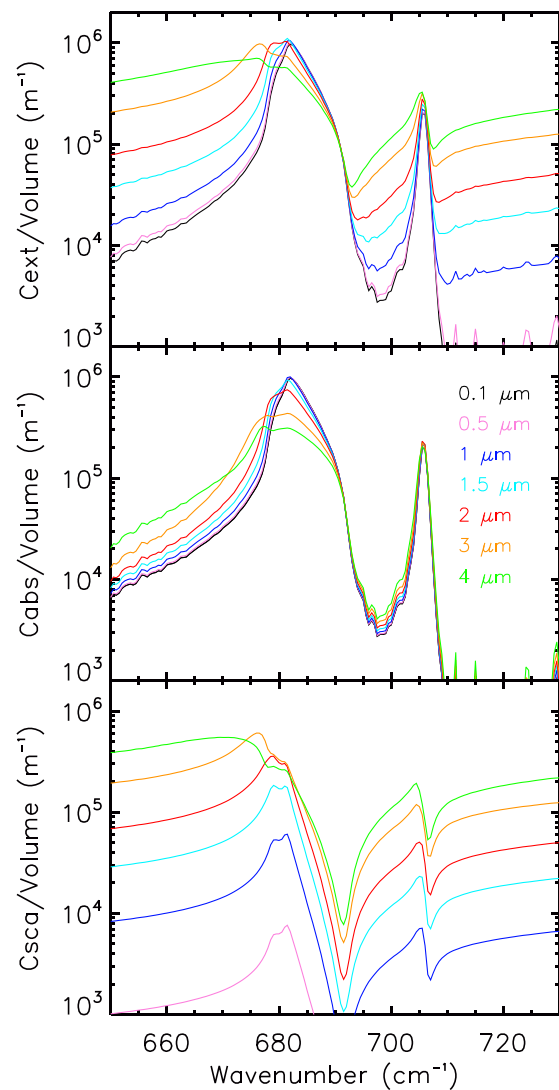


Fig. 7. Spectral dependences of the extinction (top), absorption (middle) and scattering (bottom) cross sections per unit particle volume calculated for spherical particles composed of pure C_6H_6 ice with different radii from $0.1\text{ }\mu\text{m}$ (black) to $4\text{ }\mu\text{m}$ (green). (For interpretation of the references to colour in this figure legend, the reader is referred to the web version of this article.)

6. Benzene ice mass mixing ratios

6.1. Retrieval method

Our code retrieves ice optical depth in each layer of the pressure grid from the best fit of the 682 cm^{-1} spectral signature. Retrievals were performed for both nadir and limb spectra assuming a spherical shape with a $0.5\text{-}\mu\text{m}$ radius for the C_6H_6 ice particles. As C_6H_6 ice particles appear when the C_6H_6 gas mixing ratio becomes saturated, or in other words where the mixing ratio profiles displayed in Fig. 4 intercept the saturation curve, we applied a cutoff in the a priori vertical profile of the C_6H_6 cloud optical depth at the level where C_6H_6 becomes saturated. Above this level, we assumed a zero optical depth. For the May 2013 nadir observation, this level varies from 0.03 mbar (280 km) at 87°S and 83°S to 5 mbar (120 km) at 68°S , while for March 2015 limb observations we applied a cutoff at 0.02 mbar.

Below the saturation level, we do not know the cloud vertical distribution and we cannot derive any vertical profile from nadir observations of the C_6H_6 ice spectral signature. Several slopes of

¹ <https://www.sshade.eu/>; C_6H_6 ice spectrum: https://doi.org/10.17178/SSHADE.GHOSS.EXPERIMENT_BS_20170830_001.V1

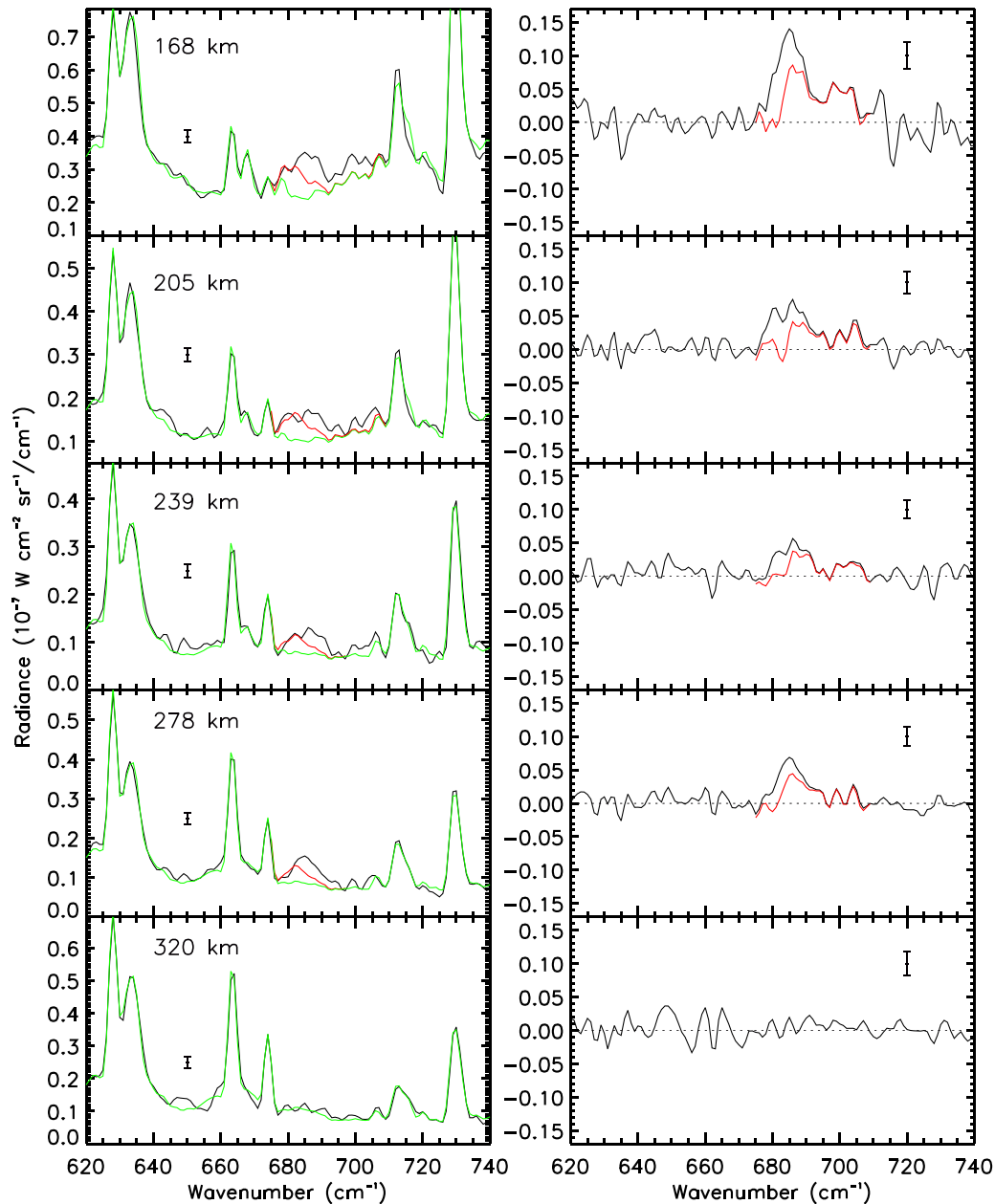


Fig. 8. CIRS limb spectra at 79°S in March 2015 (black line) of the 615–740 cm^{-1} region compared to the calculated spectra without C_6H_6 ice (green) and including it (red). Altitudes of the averaged spectra take into account the +40 km shift relatively to the altitude given in the CIRS database. Right: Corresponding residuals (observed spectrum minus calculated spectrum) without C_6H_6 ice (black) and including it (red). 1- σ error bars are given for each spectrum. (For interpretation of the references to colour in this figure legend, the reader is referred to the web version of this article.)

the vertical distribution can yield similar satisfactory fits of a nadir spectrum. We therefore first derived constraints on the vertical distribution of the cloud optical depth from the limb observations acquired in March 2015, where the 682 cm^{-1} spectral band is observed in limb spectra at 278 km and deeper (see Fig. 8).

But, as mentioned in Section 4.3, emission bands of molecular gases, which are highly enriched, generally become opaque deeper than the 0.003 mbar level (~ 360 km), like for C_6H_6 gas (see Section 4.4). It would be possible to derive information at deeper levels by using a 2-D retrieval algorithm, as performed by Achterberg et al. (2008), which would take into account the thermal and compositional meridional gradients along the limb line-of-sight. Building such a 2-D retrieval algorithm is outside the scope of this paper. Nevertheless, C_6H_6 ice band and continuum emission due to haze are optically thin at levels in the 0.03–0.6 mbar (270–

175 km) region, much deeper than the region where gas emissions are optically thin. As we are interested in retrieving the vertical distribution of the C_6H_6 ice cloud, we chose to retrieve gas mixing ratios using limb spectra deeper than 0.003 mbar individually but knowing that the retrieved gas mixing ratios were not representative of the 79°S latitude, but instead lower latitudes. The idea here is to obtain the best fit of each limb spectrum acquired below the 0.03 mbar level in order to fit the 682 cm^{-1} ice signature in a second step. Best fits of limb spectra acquired between 168 and 320 km are displayed in Fig. 8. These limb spectra were initially acquired at 0.5 cm^{-1} resolution and degraded to the spectral resolution of 2.8 cm^{-1} in order to facilitate comparison by eye with the nadir spectra of Fig. 2.

After having obtained the gas mass mixing ratio profiles that best fit the 168–320 km limb spectra in March 2015, we derived

the vertical distribution of the C_6H_6 ice cloud by fitting the 678–683 cm^{-1} region. This vertical ice cloud profile was then used as an a priori for the retrievals of the ice mixing ratio spatial distribution from nadir spectra acquired in May 2013.

6.2. Results

Figs. 2 and 8 display fits of the observed 682 cm^{-1} spectral signature in May 2013 in nadir spectra and in March 2015 in limb spectra. Residuals are displayed in the right panel of both figures without the benzene ice contribution (black line) and including it (red). In May 2013 (Fig. 2), the 682 cm^{-1} ice feature as well as the unidentified 695 cm^{-1} one are more prominent in the 80–75°S latitudinal region. The 682 cm^{-1} C_6H_6 ice spectral signature is not detectable for latitudes lower than 65°S, where the benzene gas emission at 674 cm^{-1} also disappears. In March 2015 (Fig. 8), at 79°S, the 682 cm^{-1} spectral signature is mixed with several unidentified spectral contributions in limb spectra at 168, 205 and 239 km with apparently two new spectral signatures at ~ 687 cm^{-1} and ~ 702 cm^{-1} . The 695 cm^{-1} signature, which is observed at the same latitude in May 2013 in nadir spectra, also possibly contributes to the observed emission.

We derive the C_6H_6 ice mass mixing ratio profile from the retrieved optical depth $d\tau$ in each layer of altitude thickness dz from the best fit of the observed spectra. In each layer, the number density of ice particles is equal to $d\tau/(\sigma_{682} dz)$, where σ_{682} is the extinction cross section of the ice particle at 682 cm^{-1} for a spherical particle of 0.5 μm radius (see Fig. 7). In May 2013, from the nadir data between 87°S and 68°S, at 7 mbar we derive ice number densities of 0.4 to 1.3 particles/ cm^3 , about 10 times smaller than the haze number density at the same level. In March 2015, from the limb observation, we derive at 0.7 mbar an ice particle number density of 0.4 cm^{-3} , also 10 times lower than the haze number density there. The mass of an ice particle is derived assuming a C_6H_6 ice density of 1.1 $g\ cm^{-3}$, which lies between the values 1.094 and 1.114 $g\ cm^{-3}$ measured at 138 K and 77 K, respectively (Cox et al., 1958; Bacon et al., 1964; Romanescu et al., 2010). The retrieved C_6H_6 ice mass mixing ratio profiles derived in May 2013 and March 2015 are displayed in Figs. 4 and 6 (in blue), respectively. 1- σ error envelopes on profiles derived from nadir data include contributions from noise and temperature uncertainty and those derived from limb observations additionally incorporate contribution of the vertical shift uncertainty (see Section 3.1).

Limb spectra in March 2015 probe the 0.02–5 mbar range, with lesser constraints in the 0.02–0.07 mbar range because of the poorly constrained temperature profile in this range (see Fig. 3 (b)). We can notice that the 278 km limb spectrum probes a level located close to the saturation curve (see Fig. 6), while the 320 km limb spectrum probes more than one scale height above the saturation curve, which is compatible with the fact that we do not observe the C_6H_6 ice spectral feature in this limb spectrum. In the 0.1–1 mbar region, we derive a roughly constant C_6H_6 ice mass mixing ratio of $\sim 1 \times 10^{-7}$.

In May 2013, the derived C_6H_6 ice mass mixing ratio at 10 mbar (~ 100 km), which is the level where the C_6H_6 ice thermal emission mostly comes from, seems to be constant within error bars from the South pole to 65°S and equal to $\sim (1-2) \times 10^{-8}$ (see Fig. 4).

Figs. 4 and 6 additionally display the haze mass mixing ratio profiles (orange lines) derived at the same pressure levels as the ice cloud. Calculation of the aerosol mass mixing ratio assumes particles of 3000 monomers of 0.05 μm radius each and a material density of 0.6 $g\ cm^{-3}$. For all latitudes observed in May 2013 and also in March 2015 at higher altitude, we derive that haze mass mixing ratio is always higher than the C_6H_6 ice mass mixing ratio, with a typical factor of 20–30. These similar ratios from one latitude to another and at two different dates suggest homogeneous

composition inside the south polar vortex. In March 2015, we derive quite constant-with-height C_6H_6 ice and haze mass mixing ratios profiles in the 0.1–0.7 mbar region, which is probably due to the air subsidence that bring enriched air in haze from the higher stratosphere to deeper levels and that aliment the C_6H_6 cloud with benzene gas enriched air from above.

7. Discussion

7.1. Benzene gas mixing ratio in the southern polar region in May 2013 and March 2015

It is more appropriate to work with volume mixing ratio when dealing with the gas distribution, in which case the C_6H_6 gas mass mixing ratio profiles plotted in Figs. 4 and 6 should be multiplied by a factor of 0.36 (ratio of the mean atmospheric molar mass equal to 27.79 $g\ mol^{-1}$, mostly due to N_2 , over the benzene molar mass equal to 78 $g\ mol^{-1}$) to be converted into volume mixing ratio.

In May 2013, at 87°S the corresponding volume mixing ratio is $\sim 1.5 \times 10^{-6}$ at 0.015 mbar (~ 300 km) and in March 2015, we derive an increase of the volume mixing ratio from 1×10^{-6} at 0.003 mbar (~ 370 km) to 5×10^{-6} at 1.5×10^{-4} mbar (~ 507 km).

In March 2015, the C_6H_6 gas volume mixing ratios observed at 0.003 mbar is higher by a factor of 60 than the value observed in September 2011 at 85°S at the same pressure level (Vinatier et al., 2015). As mentioned earlier, no other limb data were acquired between these dates because of highly inclined orbits of Cassini. This increase is explained by the subsidence bringing enriched air from high altitude toward deeper levels.

In May 2013 and March 2015, our derived C_6H_6 gas volume mixing ratios are comparable to the in situ values of 9×10^{-7} – 3×10^{-6} measured by the Cassini Ion and Neutral Mass Spectrometer at 1000 km (Vuitton et al., 2007; Cui et al., 2009; Magee et al., 2009). Benzene is not the only molecule to display such a high enhancement inside the polar vortex: C_2H_2 , HCN, HC_3N , C_4H_2 , CH_3CCH , C_2H_4 are also observed to be highly enriched in March 2015 above 400 km (Vinatier et al., 2016), with mixing ratios comparable to the INMS measurements around 1000 km. The highly enriched volume mixing ratios observed with CIRS inside the southern polar vortex, suggest that the vortex barrier is very efficient not only at stratospheric levels but also at much higher altitude, so that the air observed in the stratosphere around 350 km has a similar composition as the air around 1000 km.

7.2. Benzene condensation level and the altitude of the south polar cloud

In May 2013, from the nadir observations we can infer information on the altitude of the top of the cloud from the fit of the C_6H_6 gas emission band and the calculated saturation curve (see Sections 4.1 and 4.2). In order to test the impact of the a priori C_6H_6 gas mixing ratio profile on the altitude of the condensation level, we tested two types of a priori profiles: profile derived from limb spectra acquired in March 2015 (Fig. 6) extrapolated for deeper levels than the 0.003-mbar level and constant-with-height mixing ratio profiles. For both a priori profiles and at all latitudes, we derived similar condensation levels (within error bars) and similar volume mixing ratios at these pressure levels. Therefore, the tendency to observe condensation of C_6H_6 deeper and deeper while moving away from the South pole seems to be robust and is due to warmer temperature in the stratosphere for lower latitude. Thus, the C_6H_6 cloud top should be located deeper with increasing distance from the pole.

In March 2015, from the limb observations, we can estimate the altitude of the top of the C_6H_6 cloud from the altitude of the high-

est limb line-of-sight where the 682 cm^{-1} benzene ice signature is observed. From these observations, the cloud top is located near 0.025 mbar (278 km), which is similar to the condensation levels observed in May 2013 at latitudes higher than 80°S .

In May 2013, among all molecules cited above, C_6H_6 is the one that condenses at the highest altitude, with condensation occurring at ~ 0.03 mbar (~ 280 km) for a saturated volume mixing ratio of $\sim 2 \times 10^{-6}$ in the 90°S – 80°S region, which is compatible with the derived altitude of 300 km of the south polar cloud observed in mid-2012 by the Cassini ISS instrument from the south pole to 80°S (West et al., 2016) and the HCN cloud observed by Cassini/VIMS (de Kok et al., 2014). From our CIRS nadir dataset of May 2013 at 87°S , we derive a condensation level for HCN located near 0.1 mbar (~ 235 km), 45 km deeper than the C_6H_6 saturation level, with a saturated volume mixing ratio of $\sim 2 \times 10^{-6}$, which is comparable to the C_6H_6 one at ~ 0.03 mbar. Therefore, C_6H_6 ice is probably an important contributor to the composition of the upper levels of the southern fall stratospheric polar cloud.

In March 2013 at 85°S and 80°S , we observe a thermal inversion in the deep stratosphere at ~ 10 mbar, which could make the atmosphere unstable regarding convection. Additionally, West et al. (2016) mentioned convective patterns in the ISS images of the South polar cloud, which could be explained by such a thermal inversion. Fig. 3(a) shows as a black dotted line the dry adiabatic lapse rate. Comparison of slopes of the retrieved thermal profiles at 87°S and 83°S and the dry adiabat shows that no convection should occur in the cloud. Nevertheless, we recall here that the vertical resolution is very limited because of nadir geometry and it is not excluded that a steeper gradient takes place over a limited vertical range, similar to the one observed from radio occultation measurements at 74°N during the northern winter (Schinder et al., 2012).

7.3. Dependence of the C_6H_6 ice spectrum with particle size and shape

Fig. 7 shows the spectral dependences of calculated cross sections per unit particle volume for different radii of spherical particles made of pure C_6H_6 ice. For spherical particles of 0.1 and $0.5\ \mu\text{m}$ radii, extinction cross sections per unit volume are very similar. This is expected as these radii are much smaller than the observed wavelength (682 cm^{-1} corresponds to $14.7\ \mu\text{m}$) and the imaginary part of the ice refractive index is not negligible (here equal to ~ 1.5 for the maximum of the absorbing band), a case in which the calculated extinction cross section does not depend on the shape of the ice particle, but only on its equivalent volume and can be described by Equation 8.4.2 of Hanel et al. (2003). Extinction is then dominated by absorption and scattering is negligible.

For spherical particles with radii of $1.5\ \mu\text{m}$ or smaller, we derived similar fits of the observed spectra and similar ice mass mixing ratios. For radii of $2\ \mu\text{m}$ or larger, fits of the 682 cm^{-1} spectral signature were degraded as the scattering contribution increases with increasing particle radius (Fig. 7), which results in a change in the shape of the spectral band, with almost no more extinction feature at 682 cm^{-1} for a $4\ \mu\text{m}$ particle radius. In conclusion, we can set an upper limit of $\sim 1.5\ \mu\text{m}$ for the equivalent radius of C_6H_6 ice particles from fits of CIRS spectra.

In order to investigate the potential impact of the shape of the C_6H_6 ice particles, we additionally performed cross section calculations using DDSCAT 7.3 (Draine and Flatau, 1994, 2008; Flatau and Draine, 2012) with cubic, rectangular, elliptical and with two-sphere or two-ellipse shape crystals made of pure C_6H_6 ice all having the same volume as a sphere of $0.5\ \mu\text{m}$ radius. The calculated extinction cross sections per unit particle volume slightly differ in shape from the spherical case, but with no possible discrimination from the observed CIRS emission.

7.4. Benzene ice particle size and sedimentation

Satisfactory fits of CIRS spectra require C_6H_6 particles of equivalent radii smaller than $1.5\ \mu\text{m}$. All results presented here were performed for C_6H_6 ice particle equivalent radii of $0.5\ \mu\text{m}$. We can estimate theoretically the mean size of a C_6H_6 ice particle from the comparison of the condensation growth timescale (τ_{cond} , proportional to the particle radius), which is the timescale over which a particle of C_6H_6 ice increases its mass by a factor e , and the falling timescale (τ_{fall}) that include the contribution of sedimentation timescale (τ_{sed} , varying as the inverse of radius) over the saturated benzene gas scale height and the dynamical timescale (τ_{dyn}) due to the air subsidence, with $\frac{1}{\tau_{\text{fall}}} = \frac{1}{\tau_{\text{sed}}} + \frac{1}{\tau_{\text{dyn}}}$, as the falling velocity is the sum of the sedimentation speed and the subsidence velocity.

7.4.1. Dynamical timescale

Vertical transport associated with the descending branch replenishes the C_6H_6 ice cloud from the top with air enriched in C_6H_6 gas. We can estimate the dynamical timescale of this transport over one scale height from the temporal evolution of the molecular gas mixing ratios profiles, as explained in Vinatier et al. (2015). We therefore need to use profiles derived with high vertical resolution from limb observations. As before March 2015, no limb data of the South pole have been acquired since September 2011, we preferred to use the closest limb observations of September 2015 (Vinatier et al., 2016) to estimate the downward velocity in the polar vortex in the March–September 2015 period. To derive this velocity, we used the derived gas mixing ratios of C_6H_6 , HC_3N , C_4H_2 , C_3H_4 , HCN and C_2H_2 at the reference pressure of 0.008 mbar in March 2015 and infer the pressure levels at which these molecular mixing ratios were observed in September 2015. We then derived that the mean pressure level of the same air composition was observed at a pressure level 4.5 times deeper in September 2015 than in March 2015. As the mean scale height is $H \sim 45$ km at 0.02 mbar, we can derive the vertical distance over which the air moved downward equal to $H \times \ln(4.5) = 1.5 H$, corresponding to a downward vertical velocity of $\sim 4\text{ mm s}^{-1}$ and $\tau_{\text{dyn}} \sim 10^7$ s at a pressure level of 0.02 mbar. From this value, we can estimate that the vertical velocity at 0.1 mbar would be 0.8 mm s^{-1} assuming that in the 0.1–0.01 mbar the flow convergence or divergence inside the polar vortex are small. This result is in agreement with the subsidence velocities that Teanby et al. (2017) calculated in 2015 from energy balance considerations. We assume here that τ_{dyn} in May 2013 was similar to the dynamical timescale derived in 2015.

7.4.2. Sedimentation timescale

We can estimate the sedimentation timescale, corresponding to the time needed for a particle to fall over one pressure scale height, for C_6H_6 ice particles. We focus here on the 0.025 mbar pressure level (~ 285 km), which corresponds to the upper part of the C_6H_6 ice cloud observed in May 2013 at 87°S and 83°S , from nadir spectra. At this low atmospheric pressure, we first check whether the interaction between an ice particle and the ambient air should be treated as interaction with a continuum flow (particle radius \gg gas mean free path) or if the gas is too rarefied (particle radius \ll gas mean free path) in which case we have to consider the gas kinetic theory. In Titan's atmosphere, assumed here to be only made of N_2 , at 0.025 mbar and 138 K, the mean free path of a molecule is ~ 1.7 mm, which is larger by a factor of ~ 1100 (equal by definition to the Knudsen number) than the maximum ice particle radius of $1.5\ \mu\text{m}$ that was derived from our observations. We are then here in the Knudsen regime and we therefore used Eq. (19) of Rossow (1978) to estimate this sedimentation

timescale over one pressure scale height:

$$\tau_{sed} = 27\pi \rho_{atm} \left(\frac{2kT}{\pi m}\right)^{\frac{3}{2}} \frac{1}{16\rho_{ice}g^2a} \quad (1)$$

were ρ_{atm} and ρ_{ice} are the atmospheric and ice densities, respectively, m is the mass of an atmospheric molecule, g is the acceleration of gravity, a is the particle radius and T the atmospheric temperature. We used $\rho_{ice} = 1100 \text{ kg m}^{-3}$, $g = 1.1 \text{ m s}^{-2}$ determined at 285 km (altitude of the 0.025 mbar level) and a temperature of 138 K and derive $\tau_{sed} = \frac{10^6}{a}$ s, with a in μm . This corresponds to a sedimentation velocity H/τ_{sed} , where H is the pressure scale height ($\sim 38 \text{ km}$ at 0.025 mbar), of 1.9 cm s^{-1} at 0.025 mbar. τ_{sed} , which is calculated for the idealized case of a sphere should be regarded as a lower limit of the sedimentation timescale as we have no idea of the shape of the C_6H_6 ice particles: for instance, they could be elongated or possibly condense on some parts of fractal aerosols that are quite fluffy and therefore would sediment less rapidly.

7.4.3. Estimation of the particle size from falling and condensation timescales

We estimated the condensation timescale using Eq. (17) of (Rossow, 1978), which is valid in the Knudsen regime:

$$\tau_{cond}^{-1} = \frac{3\alpha f \rho_{sat} S_{max}}{2a\rho_{ice}} \left(\frac{2kT}{\pi m}\right)^{\frac{1}{2}} \quad (2)$$

where a is the particle radius, α is the molecular sticking coefficient, chosen to be equal to 0.7, which is similar to the mean H_2O sticking coefficient measured in the temperature range 190–235 K (Skrotzki et al., 2013), as no measurement of the sticking coefficient of C_6H_6 ice was found in the literature. The f parameter is equal to 3.8 and we used a supersaturation maximum $10^{-3} < S_{max} < 10^{-1}$, as suggested by Rossow (1978). ρ_{sat} is the saturation C_6H_6 vapor density.

We focus here on the nadir observation at 87°S of May 2013, where the C_6H_6 gas saturates at 0.025 mbar ($\sim 285 \text{ km}$) and 138 K and derive $\tau_{cond} = a \times 10^{6\pm 1}$ s with a in μm . If we consider that C_6H_6 condensation occurs over the saturated benzene gas scale height, i.e. ~ 0.3 pressure scale height here, then by equalizing τ_{cond} and $\tau_{fall} \times 0.3$, we obtain a range of $0.1 \mu\text{m} < a < 1.7 \mu\text{m}$ with a mean equivalent radius of $0.5 \mu\text{m}$. This is consistent with the observational constraints on the equivalent radius that we determined from the fits of the C_6H_6 ice band (Section 7.3). This estimated equivalent radius is also in agreement with the mean size of C_6H_6 ice particles of Barth (2017)'s microphysics model, which focus on equatorial conditions, where C_6H_6 condenses much deeper (around 90 km) than what we observe here.

Coagulation and coalescence processes at the C_6H_6 saturation pressure level (0.025 mbar), where the estimated ice particle number density is about 0.5 cm^{-3} , are negligible as their corresponding timescales, determined from Eqs. (33) and (37) of Rossow (1978), respectively, are two orders of magnitude higher than the sedimentation and condensation timescales.

By conservation of the mass flux we can estimate the mass mixing ratio of C_6H_6 ice (q_{ice}) from the gas mass mixing ratio at the condensation level (q_{sat}) with $q_{ice} \sim \frac{\tau_{sed}}{\tau_{sed} + \tau_{dyn}} q_{sat}$. From the estimated range of the C_6H_6 ice particle radius, τ_{sed} varies from 6.0×10^5 s to 7.3×10^5 s. This implies $0.05 < q_{ice}/q_{sat} < 0.4$, which is compatible within error bars with our derived results in May 2013 and March 2015 if we extrapolate the ice mass mixing ratios of May 2013 toward the condensation level or if we extrapolate the gas mass mixing ratio of March 2015 to the saturation level (see Figs. 4 and 6).

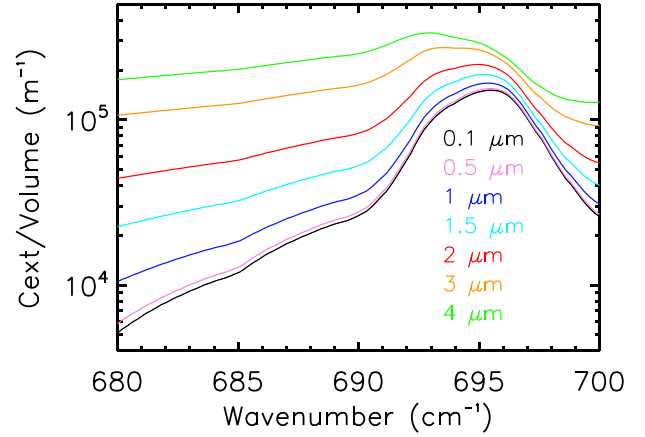


Fig. 9. Spectral dependence of the extinction cross section per unit particle volume calculated for spherical particles composed of pure $\text{C}_2\text{H}_3\text{CN}$ ice with different radii from $0.1 \mu\text{m}$ (black line) to $4 \mu\text{m}$ (green). (For interpretation of the references to colour in this figure legend, the reader is referred to the web version of this article.)

7.5. Tentative identification of other ice signatures in the 680–710 cm^{-1} range

As mentioned in Section 6.2, unidentified signatures are observed in limb spectra at 79°S near 687 cm^{-1} and 702 cm^{-1} in March 2015 (Fig. 8) at 168, 205 and 239 km. Nadir spectra of May 2013 seem to display a common signature in the $695\text{--}700 \text{ cm}^{-1}$ spectral range that is more prominent at 78°S and 73°S . These signatures are $\sim 5\text{--}10 \text{ cm}^{-1}$ large and are detected at relatively low altitude as they are only observed on the 278 km limb spectrum and deeper in nadir spectra, which probe the 5–20 mbar (150–100 km) region. This suggests possible ices as spectroscopic candidates.

7.5.1. CH_3CN and other nitrile candidates

We searched for possible ice candidates that could reproduce the observed limb spectra and that could condense at high altitude. Several nitrile ices display spectral signatures in the $650\text{--}800 \text{ cm}^{-1}$ spectral range. Moore et al. (2010) determined optical constants of several nitrile ices relevant for Titan's atmosphere. Their best candidates for our observed unidentified signature near 695 cm^{-1} is CH_3CN . In order to verify if this nitrile ice could reproduce the observed limb spectra, we used their optical constants to calculate the spectral dependence of extinction cross sections for spherical particles of radius varying from 0.01 to $1.0 \mu\text{m}$. The CH_3CN 695 cm^{-1} ice band could contribute to the 695 cm^{-1} emission feature but it should also display a stronger emission band at 773 cm^{-1} that should be detectable in CIRS limb spectra if the observed 695 cm^{-1} band intensity is reproduced. But, as we do not detect the 773 cm^{-1} CH_3CN ice feature, we can exclude a contribution of this pure ice to the CIRS observed limb spectra. Therefore, CH_3CN pure ice does not explain the observed signal at 695 cm^{-1} . The other nitriles investigated in Moore et al. (2010)'s study (HC_3N , $\text{C}_2\text{H}_5\text{CN}$, HCN , and C_2N_2) do not have any spectral signature close to 700 cm^{-1} .

7.5.2. The $\text{C}_2\text{H}_3\text{CN}$ potential candidate

Dello Russo and Khanna (1996) derived optical constants of acrylonitrile ($\text{C}_2\text{H}_3\text{CN}$) ice, which displays a single signature at 695 cm^{-1} in the mid-IR range observed by CIRS. We utilized their optical constants to derive from Mie calculation the spectral dependence of the extinction cross sections of $\text{C}_2\text{H}_3\text{CN}$ ice for spherical particles with radii varying from 0.01 to $4.0 \mu\text{m}$ (see Fig. 9). The noise level in nadir and limb spectra and the spectral contribution of the unknown spectral feature at 687 cm^{-1} in limb spec-

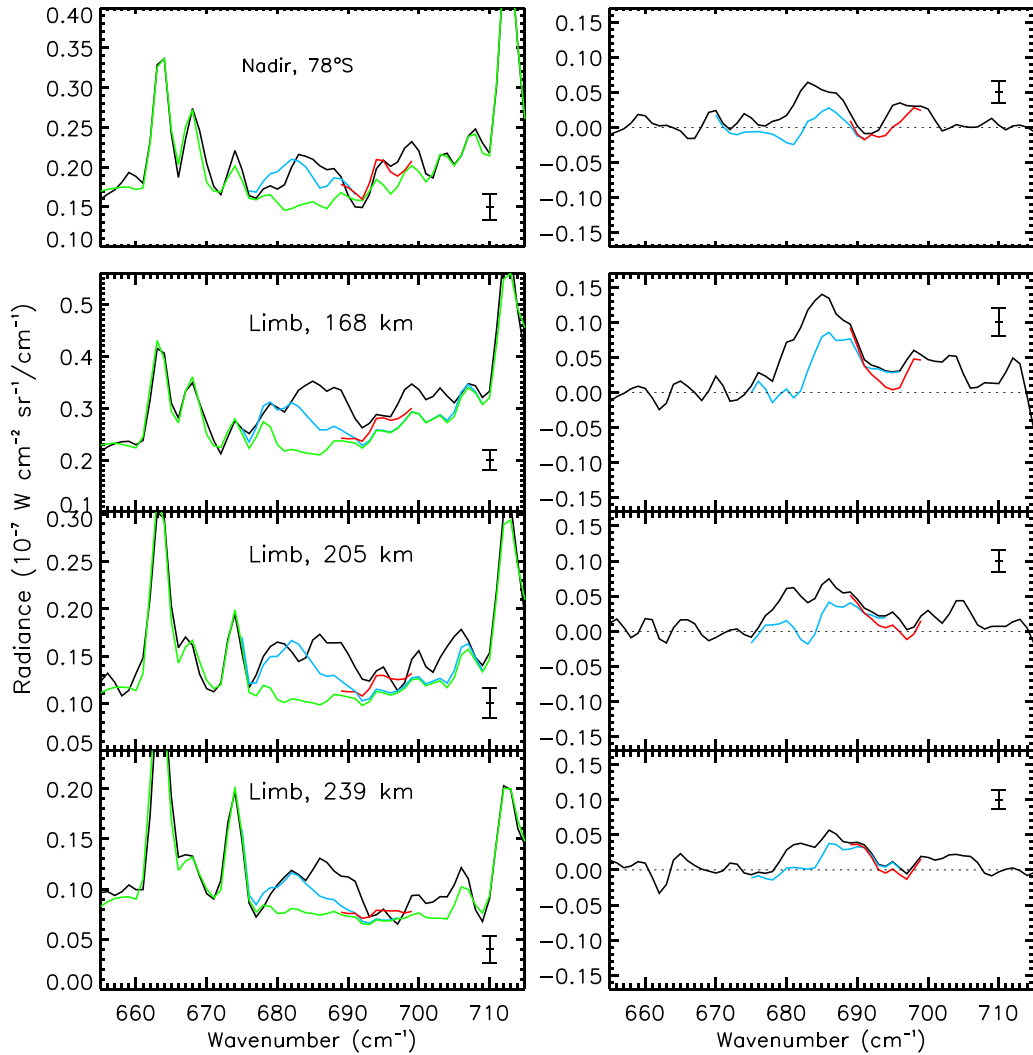


Fig. 10. Top panel: same as Fig. 2 but only for the nadir spectrum at 78°S and including the C_2H_3CN ice signature in red and C_6H_6 ice in blue. Lower panels: same as Fig. 8 but only for the limb spectra at 168, 205 and 239 km and including the C_2H_3CN ice signature in red and C_6H_6 ice in blue. (For interpretation of the references to colour in this figure legend, the reader is referred to the web version of this article.)

tra prevented us from deriving constraints on the size of the potential C_2H_3CN ice particles. We then chose to perform retrievals with the extinction cross section calculated for a particle radius of $0.5\ \mu\text{m}$ (like for C_6H_6 ice). Resulting fits of the 78°S nadir spectrum of May 2013 and the March 2015 limb spectra are displayed in Fig. 11 (a). The $695\ \text{cm}^{-1}$ signature is seen on limb spectra at 168 and 205 km, and possibly 239 km and we therefore applied a cutoff on the a priori optical depth profile of the C_2H_3CN ice at 0.05 mbar (~ 250 km). The retrieved C_2H_3CN ice mass mixing ratio profile from the 168, 205 km and 239 km limb spectra is displayed in Fig. 11 (cyan line) and probe the 0.1–1 mbar region. This vertical profile was then used to model the nadir $695\ \text{cm}^{-1}$ signature at 78°S. The resulting fit is displayed in Fig. 10 (top panel), and the retrieved mass mixing ratio at 78°S is displayed in Fig. 11 (in black). The nadir spectrum probes the 0.4–20 mbar (205–80 km) region. At 78°S, we derive a C_2H_3CN ice mass mixing ratio half that of C_6H_6 ice at 0.1 mbar and 10 times smaller at 10 mbar. Fig. 11 additionally displays the C_2H_3CN liquid-gas transition curve in Titan's atmosphere derived from data listed in Lide (2009), as no sublimation data exist in the literature. Nevertheless, the slope of the sublimation curve near the triple point, of which the temperature is 189.6 K (Lide, 2009), is always steeper than the slope of the liquid-gas curve in a phase transition pressure-temperature di-

agram. We therefore expect the sublimation curve to be located at lower pressure levels than the liquid-gas one in Fig. 11. Therefore, C_2H_3CN should condense at a pressure level lower than ~ 0.2 mbar, or altitude higher than ~ 200 km (corresponding to the level where the C_2H_3CN ice mass mixing ratio crosses the liquid-gas saturation curve). This is therefore compatible with the possible detection of C_2H_3CN ice emission feature at 239 km and below.

Acrylonitrile gas was detected by Cassini/INMS near 1000 km with volume mixing ratios varying from 3.5×10^{-7} to 1×10^{-5} (Vuitton et al., 2007; Magee et al., 2009; Cui et al., 2009) and from the Atacama Large Millimeter Array (ALMA) above 200 km with mixing ratios comprised between 0.36 and 2.83×10^{-9} at 300 km (Palmer et al., 2017). If the $695\ \text{cm}^{-1}$ signature observed in limb spectra of March 2015 is due to acrylonitrile ice and if we assume that the retrieved ice mass mixing ratio near 0.1 mbar is the one near the top of the C_2H_3CN cloud (as the $695\ \text{cm}^{-1}$ signature is not detected at higher altitude), then because of mass flux conservation, the gas volume mixing ratio at ~ 0.1 mbar should be higher than $\sim 4 \times 10^{-8}$, and also lower than the INMS values. There is currently no line list of the acrylonitrile gas in the mid-IR but Khlif et al. (1999) determined its IR spectrum, which displays many vibrational modes, and measured the corresponding integrated band intensities. In the mid-IR spectral region ob-

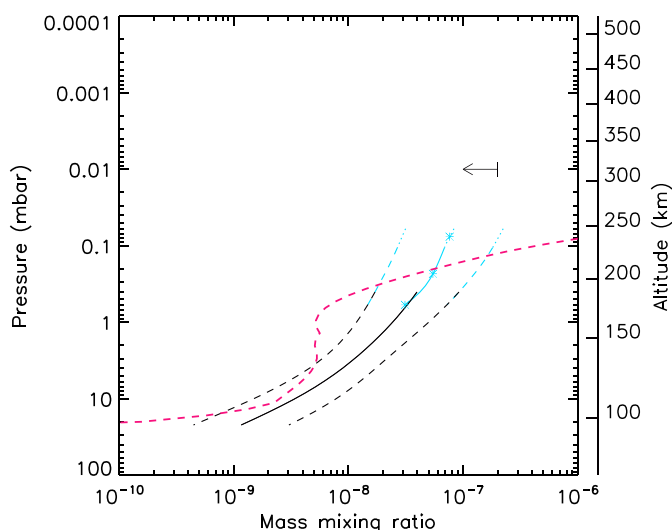


Fig. 11. Retrieved C_2H_3CN ice mass mixing ratio profile from the limb spectra (cyan line) and from the nadir spectrum at $78^\circ S$ (black). Solid lines give the mean mass mixing ratio, while dashed lines give the $1\text{-}\sigma$ error bars. Mean altitudes of the line-of-sight of the limb spectra are displayed as crosses. The pink dashed line gives the liquid-gas transition curve in Titan's atmosphere derived from Lide (2009). Arrow represents upper limit of the C_2H_3CN gas mixing ratio derived from CIRS limb observation at 0.01 mbar. (For interpretation of the references to colour in this figure legend, the reader is referred to the web version of this article.)

served by CIRS, the three most intense acrylonitrile bands are located at 682 , 953 and 972 cm^{-1} . The Q-branch of the ν_{14} bending mode of C_2H_3CN gas localized at 682 cm^{-1} is superposed to the 682 cm^{-1} spectral signature that we attributed here to the C_6H_6 ice ν_4 bending mode. Nevertheless, we can be sure that the ν_{14} C_2H_3CN gas Q-branch does not explain the 682 cm^{-1} signature because this Q-branch is only $1\text{--}2\text{ cm}^{-1}$ wide, which is not enough to reproduce the $5\text{--}10\text{ cm}^{-1}$ wide band observed here. We can estimate the 682 cm^{-1} C_2H_3CN Q-branch intensity using the Khlifi et al. (1999) integrated intensity of $41\text{ cm}^{-2}\text{ atm}^{-1}$, the HC_3N or C_6H_6 gas spectral radiance observed by CIRS (at 663 and 674 cm^{-1} , respectively), and their integrated band intensities measured by Khlifi et al. (1992a, 1992b). To do so, we use the equation $\frac{I_1}{I_2} = \frac{q_1 S_1 B_1}{q_2 S_2 B_2}$, where I_1 and I_2 are observed radiances of species 1 and 2, respectively, S_1 and S_2 the band strengths for the corresponding absorption features, q_1 and q_2 the volume mixing ratios and B_1 and B_2 the Planck radiance at the wavenumbers of the emission bands of species 1 and 2, respectively. We applied a factor $\frac{1}{3}$ to the integrated band intensities of HC_3N and C_6H_6 in order to estimate their Q-branches integrated intensities. If we assume a C_2H_3CN gas volume mixing ratio of 5×10^{-8} at 0.1 mbar ($\sim 250\text{ km}$), then it would be reasonable to estimate a mixing ratio value of the order of 1×10^{-7} at 0.01 mbar ($\sim 320\text{ km}$), which is the level above which we derive information for the molecular gas mixing ratios at limb viewing. Using the Q-branches intensities of HC_3N and C_6H_6 from the 320-km limb spectrum of Fig. 8, we then estimate that the radiance of the C_2H_3CN Q-branch would be $0.03 \times 10^{-7}\text{ W cm}^2\text{ sr}^{-1}/\text{cm}^{-1}$, which is similar to the noise equivalent spectral radiance in CIRS spectrum (see residuals in Fig. 8). Doing the same calculation for the ν_{12} and ν_{13} C_2H_3CN Q-branches at 972 and 953 cm^{-1} , respectively, which have a total integrated intensity of $201\text{ cm}^{-2}\text{ atm}^{-1}$ (two Q-branches of $\sim 100\text{ cm}^{-2}\text{ atm}^{-1}$ each) give a predicted radiance 3 times smaller than the ν_{14} one, which is not detectable here. From the noise level ($\sim 0.02 \times 10^{-7}\text{ W cm}^2\text{ sr}^{-1}/\text{cm}^{-1}$) of the 320-km limb spectrum, the corresponding $3\text{-}\sigma$ upper limit of the C_2H_3CN gas volume mixing ratio is 2×10^{-7} at 0.01 mbar at $79^\circ S$ in March 2015. If C_2H_3CN gas displays a gradient similar to other molecules (C_6H_6 , HC_3N , HCN ,

C_2H_2 , C_4H_2 and CH_3C_2H), then we would expect an increase of its volume mixing ratio by a factor ~ 10 from 0.01 to 1×10^{-4} mbar where molecule volume mixing ratios reach values comparable to INMS measurements at 1000 km. Thus, this would correspond to a C_2H_3CN gas volume mixing ratio consistent with the INMS measurements. Such a vertical volume mixing ratio profile would then be consistent with a non detection of the C_2H_3CN gas emission in CIRS spectra, while its ice emission could be detected.

7.5.3. The 687 cm^{-1} signature

We did not find in the literature any pure ice candidate that could explain the 687 cm^{-1} spectral feature. It is possible that a complex vibrational interaction with aerosols and/or other ices produces a shift in the frequency of the ice spectral signature and/or modifies the shape of the spectral signature (see for instance the case of predicted $H_2O\text{--}CO_2$ core-shell particles extinction spectra of Isenor et al. (2013)). Ongoing laboratory experiment efforts on identifying the ice mixtures that could reproduce this spectral feature are conducted at NASA/GSFC (Anderson et al., 2017).

7.5.4. Voyager observations

It is interesting to notice that Voyager limb observations of the north pole of Titan, during the northern winter, displayed several unidentified spectral signatures (Coustenis et al., 1999), and in particular the 682 cm^{-1} signature that we detect here in CIRS spectra at the south pole in the middle of fall. Coustenis et al. (1999) also detected a large spectral signature in the $690\text{--}710\text{ cm}^{-1}$ that could correspond to the 702 cm^{-1} unidentified signatures observed here. Additionally, the 700 cm^{-1} spectral signature was observed in CIRS spectra in the northern polar region during winter and we therefore may be seeing here the appearance of this signature that will remain during the entire southern winter.

8. Conclusion and perspectives

This study reports the first detection of C_6H_6 ice in Titan's atmosphere from its ν_4 C-H bending mode at 682 cm^{-1} . We have constrained the vertical profile of the benzene ice cloud in March 2015 at $79^\circ S$ and derived its spatial distribution from the south pole to $68^\circ S$ in May 2013. Top of the C_6H_6 ice cloud is observed deeper with increasing distance from the south pole, while the ice mass mixing ratio seems to be constant at ~ 10 mbar from one latitude to another. We derived an upper limit of $1.5\text{ }\mu\text{m}$ for the equivalent radius of C_6H_6 ice particles from the shape of the 682 cm^{-1} emission band, which is in agreement with our estimation of the ice particle size from condensation growth and falling timescales comparison. Observation of the C_6H_6 ice spectral signature is associated with unidentified spectral signatures observed in limb spectra in the $685\text{--}710\text{ cm}^{-1}$ spectral range in the 0.1–1 mbar region and in the $78^\circ S$ and $73^\circ S$ nadir spectra observed in May 2013. We tested several pure nitrile ices that have emission bands in this range and with available optical constants. We derived that C_2H_3CN would be the only pure nitrile ice candidate (we also tested HCN , HC_3N , CH_3CN , C_2H_5CN and C_2N_2) that could contribute in this spectral region with a band centered at 695 cm^{-1} , from which we derived an ice mass mixing ratio between 2 and 10 times smaller than the C_6H_6 ice one in the 0.1–10 mbar region. We inferred an upper limit of $\sim 2 \times 10^{-7}$ for the C_2H_3CN gas volume mixing ratio at 0.01 mbar at $79^\circ S$ in March 2015.

Even if the present paper focuses on the study of two CIRS datasets of the south pole in May 2013, from nadir viewing, and in March 2015 from limb geometry, we observed the 682 cm^{-1} spectral signature in many other southern polar nadir spectra from early 2013 to early 2015. The C_6H_6 ice emission band presents some temporal variations and the 695 cm^{-1} spectral feature, that

we tentatively attribute to the C_2H_3CN ice, is also observed in other data. A detailed study of the south polar CIRS nadir data and limb spectra acquired after March 2015 will allow us to derive more information on the formation, evolution and composition of the southern stratospheric polar cloud that appeared during the southern fall of Titan.

Acknowledgment

This work was funded by the French Centre National d'Etudes Spatiales and the Programme National de Planétologie (INSU). We thank E. Barth and C. Anderson for helpful discussions.

Supplementary material

Supplementary material associated with this article can be found, in the online version, at [10.1016/j.icarus.2017.12.040](https://doi.org/10.1016/j.icarus.2017.12.040).

References

- Achterberg, R.K., Conrath, B.J., Gierasch, P.J., Flasar, F.M., Nixon, C.A., 2008. Titan's middle-atmospheric temperatures and dynamics observed by the Cassini Composite Infrared Spectrometer. *Icarus* 194, 263–277. doi:[10.1016/j.icarus.2007.09.029](https://doi.org/10.1016/j.icarus.2007.09.029).
- Achterberg, R.K., Gierasch, P.J., Conrath, B.J., Flasar, F., Jennings, D.E., Nixon, C.A., 2014. Post-equinox variations of Titan's mid-stratospheric temperatures from Cassini/CIRS observations. AAS/Division for Planetary Sciences Meeting Abstracts. AAS/Division for Planetary Sciences Meeting Abstracts, Vol. 46.
- Achterberg, R.K., Gierasch, P.J., Conrath, B.J., Michael Flasar, F., Nixon, C.A., 2011. Temporal variations of Titan's middle-atmospheric temperatures from 2004 to 2009 observed by Cassini/CIRS. *Icarus* 211, 686–698. doi:[10.1016/j.icarus.2010.08.009](https://doi.org/10.1016/j.icarus.2010.08.009).
- Anderson, C., Nna-Mvondo, D., Samuelson, R.E., Achterberg, R.K., Flasar, F.M., Jennings, D.E., Raulin, F., 2017. Titan's high altitude south polar (HASP) stratospheric ccc cloud as observed by Cassini CIRS. AAS/Division for Planetary Sciences Meeting Abstracts. AAS/Division for Planetary Sciences Meeting Abstracts, 49, 304-10.
- Bacon, G.E., Curry, N.A., Wilson, S.A., 1964. A crystallographic study of solid benzene by neutron diffraction. *Proc. R. Soc. London, Ser. A* 279, 98–110. doi:[10.1098/rspa.1964.0092](https://doi.org/10.1098/rspa.1964.0092).
- Barth, E.L., 2017. Modeling survey of ices in Titan's stratosphere. *Planet. Space Sci.* 137, 20–31. doi:[10.1016/j.pss.2017.01.003](https://doi.org/10.1016/j.pss.2017.01.003).
- Bertie, J.E., Keefe, C.D., 2004. Infrared intensities of liquids XXIV: optical constants of liquid benzene- h_6 at 25 °C extended to 11.5 cm^{-1} and molar polarizabilities and integrated intensities of benzene- h_6 between 6200 and 11.5 cm^{-1} . *J. Mol. Struct.* 695, 39–57. doi:[10.1016/j.molstruc.2003.11.002](https://doi.org/10.1016/j.molstruc.2003.11.002).
- Bézar, B., Vinatier, S., Achterberg, R., 2018. Seasonal radiative modeling of Titan's stratospheric temperatures at low latitudes. *Icarus* 302, 437–450. doi:[10.1016/j.icarus.2017.11.034](https://doi.org/10.1016/j.icarus.2017.11.034).
- Coustenis, A., Jennings, D.E., Achterberg, R.K., Bampasidis, G., Lavvas, P., Nixon, C.A., Teanby, N.A., Anderson, C.M., Cottini, V., Flasar, F.M., 2016. Titan's temporal evolution in stratospheric trace gases near the poles. *Icarus* 270, 409–420. doi:[10.1016/j.icarus.2015.08.027](https://doi.org/10.1016/j.icarus.2015.08.027).
- Coustenis, A., Schmitt, B., Khanna, R.K., Trotta, F., 1999. Plausible condensates in Titan's stratosphere from Voyager infrared spectra. *Planet. Space Sci.* 47, 1305–1329. doi:[10.1016/S0032-0633\(99\)00053-7](https://doi.org/10.1016/S0032-0633(99)00053-7).
- Cox, E.G., Cruickshank, D.W.J., Smith, J.A.S., 1958. The crystal structure of benzene at $-3^\circ C$. *Proc. R. Soc. London, Ser. A* 247, 1–21. doi:[10.1098/rspa.1958.0167](https://doi.org/10.1098/rspa.1958.0167).
- Cui, J., Yelle, R.V., Vuitton, V., Waite, J.H., Kasprzak, W.T., Gell, D.A., Niemann, H.B., Müller-Wodarg, I.C.F., Borggren, N., Fletcher, G.G., Patrick, E.L., Raaen, E., Magee, B.A., 2009. Analysis of Titan's neutral upper atmosphere from Cassini Ion Neutral Mass Spectrometer measurements. *Icarus* 200, 581–615. doi:[10.1016/j.icarus.2008.12.005](https://doi.org/10.1016/j.icarus.2008.12.005).
- de Kok, R., Irwin, P.G.J., Teanby, N.A., 2008. Condensation in Titan's stratosphere during polar winter. *Icarus* 197, 572–578. doi:[10.1016/j.icarus.2008.05.024](https://doi.org/10.1016/j.icarus.2008.05.024).
- de Kok, R., Irwin, P.G.J., Teanby, N.A., Nixon, C.A., Jennings, D.E., Fletcher, L., Howett, C., Calcutt, S.B., Bowles, N.E., Flasar, F.M., Taylor, F.W., 2007. Characteristics of Titan's stratospheric aerosols and condensate clouds from Cassini CIRS far-infrared spectra. *Icarus* 191, 223–235. doi:[10.1016/j.icarus.2007.04.003](https://doi.org/10.1016/j.icarus.2007.04.003).
- de Kok, R.J., Teanby, N.A., Maltagliati, L., Irwin, P.G.J., Vinatier, S., 2014. HCN ice in Titan's high-altitude southern polar cloud. *Nature* 514, 65–67. doi:[10.1038/nature13789](https://doi.org/10.1038/nature13789).
- Dello Russo, N., Khanna, R.K., 1996. Laboratory infrared spectroscopic studies of crystalline nitriles with relevance to outer planetary systems. *Icarus* 123, 366–395. doi:[10.1006/icar.1996.0165](https://doi.org/10.1006/icar.1996.0165).
- Draine, B.T., Flatau, P.J., 1994. Discrete-dipole approximation for scattering calculations. *J. Opt. Soc. Am. A* 11, 1491–1499. doi:[10.1364/JOSAA.11.001491](https://doi.org/10.1364/JOSAA.11.001491).
- Draine, B.T., Flatau, P.J., 2008. Discrete-dipole approximation for periodic targets: theory and tests. *J. Opt. Soc. Am. A* 25, 2693. doi:[10.1364/JOSAA.25.002693](https://doi.org/10.1364/JOSAA.25.002693). 0809.0338.
- Flatau, P.J., Draine, B.T., 2012. Fast near field calculations in the discrete dipole approximation for regular rectilinear grids. *Opt. Express* 20, 1247. doi:[10.1364/OE.20.001247](https://doi.org/10.1364/OE.20.001247).
- Fray, N., Schmitt, B., 2009. Sublimation of ices of astrophysical interest: a bibliographic review. *Planet. Space Sci.* 57, 2053–2080. doi:[10.1016/j.pss.2009.09.011](https://doi.org/10.1016/j.pss.2009.09.011).
- Hanel, R.A., Conrath, B.J., Jennings, D.E., Samuelson, R.E., 2003. *Exploration of the Solar System by Infrared Remote Sensing*, Second ed. Cambridge University Press, 2003, Cambridge, UK. ISBN 0521818974.
- Izenor, M., Escribano, R., Preston, T.C., Signorell, R., 2013. Predicting the infrared band profiles for CO_2 cloud particles on Mars. *Icarus* 223, 591–601. doi:[10.1016/j.icarus.2013.01.009](https://doi.org/10.1016/j.icarus.2013.01.009).
- Jennings, D.E., Anderson, C.M., Samuelson, R.E., Flasar, F.M., Nixon, C.A., Bjoraker, G.L., Romani, P.N., Achterberg, R.K., Cottini, V., Hesman, B.E., Kunde, V.G., Carlson, R.C., de Kok, R., Coustenis, A., Vinatier, S., Bampasidis, G., Teanby, N.A., Calcutt, S.B., 2012. First observation in the south of Titan's far-infrared 220 cm^{-1} cloud. *Astrophys. J.* 761, L15. doi:[10.1088/2041-8205/761/1/L15](https://doi.org/10.1088/2041-8205/761/1/L15).
- Khlifi, M., Nollet, M., Paillous, P., Bruston, P., Raulin, F., Bénilan, Y., Khanna, R.K., 1999. Absolute intensities of the infrared bands of gaseous acrylonitrile. *J. Molec. Spec.* 194, 206–210. doi:[10.1006/jmsp.1998.7795](https://doi.org/10.1006/jmsp.1998.7795).
- Khlifi, M., Raulin, F., Dang-Nhu, M., 1992. Benzene ν_4 integrated band intensity versus temperature. *J. Molec. Spec.* 154, 235–239. doi:[10.1016/0022-2852\(92\)90203-Z](https://doi.org/10.1016/0022-2852(92)90203-Z).
- Khlifi, M., Raulin, F., Dang-Nhu, M., 1992. Integrated band intensity versus temperature for the ν_1 , ν_2 , ν_3 , and ν_6 bands of cyanoacetylene. *J. Mol. Spectrosc.* 155, 77–83. doi:[10.1016/0022-2852\(92\)90549-4](https://doi.org/10.1016/0022-2852(92)90549-4).
- Larson, E.J.L., Toon, O.B., Friedson, A.J., 2014. Simulating Titan's aerosols in a three dimensional general circulation model. *Icarus* 243, 400–419. doi:[10.1016/j.icarus.2014.09.003](https://doi.org/10.1016/j.icarus.2014.09.003).
- Lebonnois, S., Burgalat, J., Rannou, P., Charnay, B., 2012. Titan global climate model: a new 3-dimensional version of the IPSL titan GCM. *Icarus* 218, 707–722. doi:[10.1016/j.icarus.2011.11.032](https://doi.org/10.1016/j.icarus.2011.11.032).
- Lide, D.R., 2009. *CRC Handbook of Chemistry and Physics: A Ready-Reference Book of Chemical and Physical Data*.
- Magee, B.A., Waite, J.H., Mandt, K.E., Westlake, J., Bell, J., Gell, D.A., 2009. INMS-derived composition of Titan's upper atmosphere: analysis methods and model comparison. *Planet. Space Sci.* 57, 1895–1916. doi:[10.1016/j.pss.2009.06.016](https://doi.org/10.1016/j.pss.2009.06.016).
- Moore, M.H., Ferrante, R.F., Moore, W.J., Hudson, R., 2010. Infrared spectra and optical constants of nitrile ices relevant to Titan's atmosphere. *Astrophys. J. Supp.* 191, 96–112. doi:[10.1088/0067-0049/191/1/96](https://doi.org/10.1088/0067-0049/191/1/96).
- Newman, C.E., Lee, C., Lian, Y., Richardson, M.I., Toigo, A.D., 2011. Stratospheric superrotation in the TitanWRF model. *Icarus* 213, 636–654. doi:[10.1016/j.icarus.2011.03.025](https://doi.org/10.1016/j.icarus.2011.03.025).
- Niemann, H.B., Atreya, S.K., Demick, J.E., Gautier, D., Haberman, J.A., Harpold, D.N., Kasprzak, W.T., Lunine, J.I., Owen, T.C., Raulin, F., 2010. Composition of Titan's lower atmosphere and simple surface volatiles as measured by the Cassini-Huygens probe gas chromatograph mass spectrometer experiment. *J. Geophys. Res. (Planets)* 115, 12006. doi:[10.1029/2010JE003659](https://doi.org/10.1029/2010JE003659).
- Palmer, M.Y., Cordiner, M.A., Nixon, C.A., Charnley, S.B., Teanby, N.A., Kiesel, Z., Irwin, P.G.J., Mumma, M.J., 2017. ALMA detection and astrobiological potential of vinyl cyanide on Titan. *Sci. Adv.* 3, e1700022. doi:[10.1126/sciadv.1700022](https://doi.org/10.1126/sciadv.1700022).
- Quirico, E., Schmitt, B., 1997. Near-infrared spectroscopy of simple hydrocarbons and carbon oxides diluted in solid n_2 and as pure ices: implications for triton and pluto. *Icarus* 127, 354–378. doi:[10.1006/icar.1996.5663](https://doi.org/10.1006/icar.1996.5663).
- Romanescu, C., Marschall, J., Kim, D., Khatiwada, A., Kalogerakis, K.S., 2010. Refractive index measurements of ammonia and hydrocarbon ices at 632.8 nm. *Icarus* 205, 695–701. doi:[10.1016/j.icarus.2009.08.016](https://doi.org/10.1016/j.icarus.2009.08.016).
- Rossov, W.B., 1978. Cloud microphysics - analysis of the clouds of Earth, Venus, Mars, and Jupiter. *Icarus* 36, 1–50. doi:[10.1016/0019-1035\(78\)90072-6](https://doi.org/10.1016/0019-1035(78)90072-6).
- Schinder, P.J., Flasar, F.M., Marouf, E.A., French, R.G., McGhee, C.A., Kliore, A.J., Rappaport, N.J., Barbinis, E., Fleischman, D., Anabtawi, A., 2012. The structure of Titan's atmosphere from Cassini radio occultations: Occultations from the Prime and Equinox missions. *Icarus* 221, 1020–1031. doi:[10.1016/j.icarus.2012.10.021](https://doi.org/10.1016/j.icarus.2012.10.021).
- Schmitt, B., Vinatier, S., Bernard, J.M., 2015. Mid-IR optical constants of crystalline C_6H_6 at 130K. Version 1. SSHADE Solid Spectroscopy database infrastructure/GhoSST (OSUG Data Center). Dataset/Spectral Data. https://doi.org/10.17178/SSHADE.GHOSST/EXPERIMENT_BS_20170830_001.
- Skrotzki, J., Connolly, P., Schnaiter, M., Saathoff, H., Möhler, O., Wagner, R., Niemand, M., Ebert, V., Leisner, T., 2013. The accommodation coefficient of water molecules on ice - cirrus cloud studies at the AIDA simulation chamber. *Atmos. Chem. Phys.* 13, 4451–4466. doi:[10.5194/acp-13-4451-2013](https://doi.org/10.5194/acp-13-4451-2013).
- Teanby, N.A., Bézar, B., Vinatier, S., Sylvestre, M., Nixon, C.A., Irwin, P.G.J., de Kok, R., Calcutt, S., Flasar, F.M., 2017. The formation and evolution of Titan's winter polar vortex. *Nature Comm.* 8, 1586. doi:[10.1038/s41467-017-01839-z](https://doi.org/10.1038/s41467-017-01839-z).
- Teanby, N.A., Irwin, P.G.J., Nixon, C.A., de Kok, R., Vinatier, S., Coustenis, A., Sefton-Nash, E., Calcutt, S.B., Flasar, F.M., 2012. Active upper-atmosphere chemistry and dynamics from polar circulation reversal on Titan. *Nature* 491, 732–735. doi:[10.1038/nature11611](https://doi.org/10.1038/nature11611).
- Vinatier, S., Bézar, B., Fouchet, T., Teanby, N.A., de Kok, R., Irwin, P.G.J., Conrath, B.J., Nixon, C.A., Romani, P.N., Flasar, F.M., Coustenis, A., 2007a. Vertical abundance profiles of hydrocarbons in Titan's atmosphere at $15^\circ S$ and $80^\circ N$ retrieved from Cassini/CIRS spectra. *Icarus* 188, 120–138. doi:[10.1016/j.icarus.2006.10.031](https://doi.org/10.1016/j.icarus.2006.10.031).
- Vinatier, S., Bézar, B., Lebonnois, S., Teanby, N.A., Achterberg, R.K., Gorius, N., Mamoutkine, A., Guandique, E., Jolly, A., Jennings, D.E., Flasar, F.M., 2015. Seasonal variations in Titan's middle atmosphere during the northern spring derived from Cassini/CIRS observations. *Icarus* 250, 95–115. doi:[10.1016/j.icarus.2014.11.019](https://doi.org/10.1016/j.icarus.2014.11.019).

- Vinatier, S., Bézard, B., Nixon, C.A., Mamoutkine, A., Carlson, R.C., Jennings, D.E., Guandique, E.A., Teanby, N.A., Bjoraker, G.L., Michael Flasar, F., Kunde, V.G., 2010. Analysis of Cassini/CIRS limb spectra of Titan acquired during the nominal mission. I. Hydrocarbons, nitriles and CO₂ vertical mixing ratio profiles. *Icarus* 205, 559–570. doi:[10.1016/j.icarus.2009.08.013](https://doi.org/10.1016/j.icarus.2009.08.013).
- Vinatier, S., Bézard, B., Teanby, N.A., Lebonnois, S., Achterberg, R., Gorius, N., Mamoutkine, A., Flasar, F.M., CIRS Team, 2016. Seasonal variations in Titan's stratosphere observed with Cassini/CIRS after the northern spring equinox. In: *AAS/Division for Planetary Sciences Meeting Abstracts*. In: *AAS/Division for Planetary Sciences Meeting Abstracts*, 48, p. 509.09.
- Vinatier, S., Rannou, P., Anderson, C.M., Bézard, B., de Kok, R., Samuelson, R.E., 2012. Optical constants of Titan's stratospheric aerosols in the 70–1500 cm⁻¹ spectral range constrained by Cassini/CIRS observations. *Icarus* 219, 5–12. doi:[10.1016/j.icarus.2012.02.009](https://doi.org/10.1016/j.icarus.2012.02.009).
- Vuitton, V., Yelle, R.V., McEwan, M.J., 2007. Ion chemistry and N-containing molecules in Titan's upper atmosphere. *Icarus* 191, 722–742. doi:[10.1016/j.icarus.2007.06.023](https://doi.org/10.1016/j.icarus.2007.06.023).
- West, R.A., Del Genio, A.D., Barbara, J.M., Toledo, D., Lavvas, P., Rannou, P., Turtle, E.P., Perry, J., 2016. Cassini imaging science subsystem observations of Titan's south polar cloud. *Icarus* 270, 399–408. doi:[10.1016/j.icarus.2014.11.038](https://doi.org/10.1016/j.icarus.2014.11.038).